Validation of earthquake ground-motion models in southern California using precariously balanced rocks

Anna H. Rood[1], Dylan H. Rood[2,3], Greg Balco[4], Peter J. Stafford[1], Lisa Grant Ludwig[5], Katherine J. Kendrick[6], Klaus M. Wilcken[7]

[1]*Department of Civil and Environmental Engineering, Imperial College London, London, SW7 2AZ, UK*

[2]*Department of Earth Science and Engineering, Imperial College London, London, SW7 2AZ, UK*

[3]*Earth Research Institute, University of California, Santa Barbara, California 93106, USA*

[4]*Berkeley Geochronology Center, Berkeley, California 94709, USA*

[5] *Department of Population Health & Disease Prevention, University of California, Irvine, California 92697, USA*

[6] *U.S. Geological Survey, Earthquake Science Center, Pasadena, California 91106, USA (emeritus)*

[7] *Australian Nuclear Science and Technology Organisation, Lucas Heights, NSW, Australia*

ABSTRACT

Accurate estimates of earthquake ground shaking rely on uncertain ground-motion models derived from limited instrumental recordings of historical earthquakes. A critical issue is that there is currently no method to empirically validate the resultant ground-motion estimates of these models at the timescale of rare, large earthquakes; this lack of validation causes large uncertainty in ground-motion estimates. Here, we address this issue and validate ground-motion estimates for southern California utilizing the unexceeded ground motions recorded by 20 precariously balanced rocks. We used cosmogenic ^{10}Be exposure dating to model the age of the precariously balanced rocks, which ranged from ~1 to ~50 ka, and calculated their probability of toppling at different ground-motion levels. With this rock data, we then validated the earthquake ground motions estimated by the UCERF3 seismic source characterization and the NGA-West2 ground-motion models. We found that no ground-motion model estimated levels of earthquake ground shaking consistent with the observed survival of all 20 precariously balanced rocks. The ground-motion model I14 estimated ground-motion levels that were rejected by the most rocks, and, therefore, I14 was invalidated and removed. At a 2475 year mean return period, the removal of this invalid ground-motion model resulted in a 2-7% reduction in the mean and a 10-36% reduction in the 5th–95th fractile uncertainty of the ground-motion estimates. Our findings demonstrate the value of empirical data from precariously balanced rocks as a validation tool to remove invalid ground-motion models and, in turn, reduce the uncertainty in earthquake ground-motion estimates.

INTRODUCTION

Earthquakes pose a present and future hazard to the population, economy, and environment in seismically active regions worldwide. California, the most populous and one of the most seismically active states in the United States, has a known history of large, damaging earthquakes, yet the impact of shaking caused by future earthquake is highly uncertain. For example, a magnitude 7.8 earthquake on the southern San Andreas fault is modeled to cause about 1,800 deaths and $213 billion of economic losses (Jones et al., 2008), yet uncertainty in these consequences impedes preparation for such an event. Probabilistic Seismic Hazard Analysis (PSHA) is the ubiquitous framework used worldwide to estimate the frequency with which a level of earthquake ground shaking will be exceeded during a given time period (Cornell, 1968; SSHAC, 2012). One fundamental component of a PSHA model is the ground motion characterization (GMC), which consists of ground-motion models (GMMs) that estimate the levels of earthquake ground shaking. However, these GMMs are derived from only several decades of instrumental recordings of historical earthquakes, which are then extrapolated to timescales for which there is essentially no constraining data. Furthermore, the limited number of instrumental recordings of historical earthquakes necessitates the assumption that the distribution of ground motions over time at a single point is the same as the distribution of ground motions in space (Anderson & Brune, 1999). Hundreds of published GMMs exist that each invariably result in a different estimation of future earthquake ground shaking (Douglas & Edwards, 2016). The inherent lack of data and knowledge about earthquake processes creates uncertainty in ground-motion estimation because multiple GMMs are considered in the PSHA model; this uncertainty is potentially major and, therefore, problematic (Gerstenberger et al., 2020). This problem is particularly acute given that these PSHA estimates of future earthquakes are crucial in land use planning, building-code revisions, disaster preparation and recovery, emergency response, and the siting, design, and maintenance of critical facilities.

Despite the importance of the PSHA results, seismic hazard estimates of future rare, large earthquakes are uncertain and unvalidated over timescales of 1,000s and 10,000s years. Currently, the challenge of selecting a suitable suite of GMMs to be used in the PSHA model is achieved by selection criteria such as those of Bommer et al. (2010). These intentionally non-specific and flexible GMM selection criteria systematically eliminate unsuitable GMMs from a complete list of available GMMs based on requirements of the rigor of modeling. Crucially, there are currently no criteria to empirically test the resultant ground-motion estimates of these GMMs at the timescale of rare, large earthquakes. A tangible solution to reduce the epistemic uncertainty in ground-motion estimates is to eliminate GMMs from the PSHA model because their ground-motion estimates can be invalidated by independent data over these timescales.

The other fundamental component of a PSHA model, in addition to a ground motion characterization, is a seismic source characterization, which consists of models that describe the location, geometry, magnitude and frequency distribution of all possible earthquake ruptures on local active faults. In southern California, the relative motion of the Pacific and North American plates, at a rate of 50.2 ± 1.1 mm yr^{-1} toward N35.8°W ± 0.2 (1σ) (DeMets et al., 2010), has produced a complicated configuration of active faults (Figure 1). These faults include multiple dextral strike-slip faults of the San Andreas fault system (SAFS) and Eastern California shear zone (ECSZ), thrust and reverse faults within the Transverse Ranges, and left-lateral faults of the Eastern Transverse Ranges. In the past 200 years the southern SAFS has produced two major earthquakes: Wrightwood in 1812 (Mw = 7.5) and Fort Tejon in 1857 (Mw = 7.9) (Jacoby et al., 1988; Sieh et al., 1989; Zielke et al., 2012). The more recent 1992 Landers (Mw = 7.3), 1999 Hector Mine (Mw = 7.1), and 2019 Ridgecrest (Mw = 7.1) earthquakes showed that the ECSZ is also capable of producing large earthquake events (DuRoss et al., 2020). In addition, the 1994 Northridge earthquake (Mw = 6.7) in the Transverse Ranges indicated the seismic hazard potential of this region (Hauksson et al., 1995). Despite many years of extensive studies, the distribution of late Quaternary strain between the various faults of the complex plate boundary zone is unresolved (Dolan et al., 2007; Powell & Weldon, 1992). This uncertainty is problematic when making hazard estimates of the size and location of future large earthquakes in southern California.

The pattern of plate boundary deformation in southern California also controls the geology, topography, and geomorphology in the vicinity of the Transverse Ranges (Figure 1). The Transverse Ranges, i.e., the San Gabriel and San Bernadino Mountains, are predominantly composed of

Precambrian and Mesozoic metamorphic and granitic rocks. The geomorphology of the San Bernadino Mountains is characterized by a high-elevation, low-relief surface, mantled by deeply weathered granite saprolite formed by weathering under a more humid Miocene climate (Oberlander, 1972). This broad erosion surface was preserved at the initiation of uplift when tectonic activity was transferred onto the current trace of the San Andreas Fault at ~7 Ma (Blythe et al., 2000). Uplift initiated river canyon incision propagating headward into the low-relief interior of the ranges. The incision has generated a landscape in disequilibrium as it transitions from a saprolite-mantled, low-relief landscape to a bedrock-dominated, high-relief landscape. While the low-relief surface in the upper reaches of catchments remain covered by regolith and saprolite, the lower reaches have eroded and removed the saprolite to exhume abundant granitic corestones that form precariously balanced rocks.

Precariously balanced rocks (PBRs) are naturally occurring inverse seismometers that record an upper limit on the ground-shaking level experienced at a site over the lifetime of the PBR, often the past 1,000s to 10,000s of years. Previous research has established methods to evaluate the probability of toppling for the rocks at various levels of ground shaking (the fragility of a rock) (Anooshehpoor et al., 2004; Purvance et al., 2008a) and the length of time the rocks have been precariously preserved in the landscape (the fragility age of a rock) (Balco et al., 2011; Bell et al., 1998). The potential to constrain PSHA estimates with these precariously balanced rock data was demonstrated at the previously proposed United States (US) high-level nuclear waste repository at Yucca Mountain (Baker et al., 2013; Hanks et al., 2013). Recently, it has been shown that precariously balanced rocks are a powerful tool to improve PSHA models and dramatically reduce uncertainties by validating each of the estimates output from the PSHA model (Rood et al., 2020; Stirling et al., 2021). Precariously balanced rocks have been identified to naturally occur across southern California with the potential to place ground-motion constraints in this seismically active region (Brune, 1996; Purvance et al., 2008b). However, neither a combined rigorous assessment of the fragility and fragility age of the rocks nor hazard model validation has been previously conducted.

The objective of the present work is to use the Third Uniform California Earthquake Rupture Forecast (UCERF3; (Field et al., 2013)) seismic source characterization and validate the Next Generation Attenuation Relationships for the Western US (NGA-West2; (Bozorgnia et al., 2014)) GMMs, both used in the 2014 and 2018 U.S. Geological Survey (USGS) National Seismic Hazard Model for California, with the unexceeded ground motions recorded by precariously balanced rocks. Our enhanced approach investigates precariously balanced rocks covering a large spatial area to validate the PSHA model outputs with multiple rocks and sites. Finally, we analyze which of the GMMs generate the ground-motion estimates that are inconsistent with the empirical precariously balanced rock data. We demonstrate how the removal of the invalid GMMs from the PSHA model ground motion characterization can reduce the uncertainty in the ground-motion estimates.

METHODS

Collectively over the past two decades, we have carried out extensive field studies across southern California to compile precariously balanced rock data (e.g., Brune (1996); Grant Ludwig et al. (2015)). During this period, the PBR selection criteria often differed between studies that focused only on characterizing PBR fragility and studies that focused only on characterizing PBR fragility age. Therefore, some of the PBRs characterized in southern California are well suited and, consequently, well characterized for either fragility or fragility age, but not both. Over this same period, however, both fragility and fragility age methods have evolved and been refined. Here, we advance previous work and rigorously characterize both the fragility and fragility age of 20 precariously balanced rocks to validate earthquake ground-motion estimates for southern California (Figure 1; Table 1).

Our fragility and fragility age methods are based on the geomorphic model that these PBRs formed as granitic corestones, which developed in the subsurface by weathering along bedrock joints and fractures, that were then exhumed by the stripping of surrounding regolith and saprolite (Oberlander, 1972). Previous textural, mineralogical, and geochemical analyses of one of our studied PBRs (RT1) concluded that this PBR was exhumed intact, and that, since exhumation, little additional fracturing or weathering has taken place (Hall et al., 2019). Additionally, Rood et al. (2020) calculated negligible erosion of studied PBR outcrops. Importantly, this supports our assumption that the present observed geometry of the studied PBRs is unchanged since the time of formation and, therefore, we can accurately assess both the fragility and fragility age of the rocks.

PBR Fragility

We define the fragility of a precariously balanced rock as the probability of it toppling given an intensity of ground motion. This probabilistic fragility definition, as opposed to a deterministic fragility, is to allow for uncertainty in the toppling of each rock due to the random variability in earthquake ground motions. The ground-motion intensity measures we used in our analysis were peak ground acceleration (PGA) and the ratio of peak ground velocity (PGV) to PGA (i.e., PGV/PGA). The use of two intensity measures results in a vector fragility analysis. A probabilistic fragility was determined for each precariously balanced rock following the methods of Rood et al. (2020) and probability of toppling equations of Purvance et al. (2008a).

The probability of a PBR toppling due to earthquake ground shaking is controlled by the geometry of the rock, specifically the radius (R) that connects the center of mass of the PBR and the basal rocking point and the angle (α) between the radius and vertical about the center of mass (Anooshehpoor et al., 2004). The geometry of each PBR was accurately described as a triangulated 3-D model produced using the photogrammetry software *PhotoModeler* (Anooshehpoor et al., 2013; PhotoModeler Technologies, 2018; Rood et al., 2020) (Figure 2A). The two critical rocking points for toppling, carefully selected in MATLAB (The Mathworks Inc, 2016), were those that defined the narrowest base in a 2-D section through the center of mass of the rock. The α and R value associated with each of the two critical rocking points were calculated, where α_1 and R_1 are measured in the most fragile direction, i.e., the direction in which the PBR will topple during earthquake ground shaking. α_2 and R_2 are measured in the conjugate rocking direction (Figure 2B). A difference in the α_1 and α_2 values of the two rocking points of less than 5% was used to classify the geometry of each PBR as symmetric and thus have as associated symmetric rocking response. Conversely, a difference in the α_1 and α_2 values of the two rocking points of greater than 5% was used to classify the geometry of each PBR as asymmetric and thus have as associated asymmetric rocking response (Rood et al., 2020).

The probability of each PBR toppling was calculated across a range of PGA and PGV/PGA values using the equations of Purvance et al. (2008a) with final coefficient corrected by Rood et al. (2020). These equations combine the geometry of the PBR (α and R) with the amplitude of the ground-motion excitation force on the PBR (PGA) and the qualities of the ground motion that dictate the period of time that a PBR is forced to tip in one direction (PGV/PGA). The distribution of PGV/PGA values that we used in the Purvance et al. (2008a) equations for each PGA level investigated was calculated using the conditional PGV model, based on PGA, of Abrahamson and Bhasin (2020). Importantly, our use of the "true mean" UCERF3 seismic source characterization precluded the disaggregation of our PSHA model in order to determine the appropriate magnitude and distance values to be used in the conditional PGV model for each PGA level. Therefore, we instead used the mean magnitude and distance values associated with the longest return period scenario available from the USGS NSHMP online Unified Hazard Tool (2475 year mean return period; https://earthquake.usgs.gov/hazards/interactive) for all PGA levels. The 2475 year mean return period is the available return period of greatest relevance for the toppling of the PBRs (Rood et al., 2020).

Finally, the median probability of toppling across the PGV/PGA distribution for each PGA value was calculated to give the probability of failure of each PBR, which we define as the fragility function of the PBR based only on PGA (Figure 2C). The different combinations of PGV/PGA, as well as their relative likelihoods, that arise for different levels of PGA are directly accounted for when reducing the vector hazard space to scalar hazard space. The slopes of the calculated fragility functions reflect the variability of the seismic capacity of each PBR and the influence of PGV on the failure of the PBR is reflected in that variability. We conducted a sensitivity analysis on the fragility function median by using the 475, 975, and 2475 year mean return period mean magnitudes and distances. This analysis showed that for most PBRs the fragility functions were insensitive to the mean magnitude and distances at the different return periods.

PBR Fragility Age

We define the fragility age of a corestone PBR as the time when the PBR-pedestal contact became exhumed by erosion of the surrounding regolith and, therefore, the PBR with its current fragile geometry became free to rock about its rocking points and potentially topple due to earthquake ground shaking. We used cosmogenic-nuclide exposure dating (Dunai, 2010), specifically the isotope ^{10}Be, to not only determine the fragility age of each of the studied PBRs but also model the rate of the erosional processes that formed each PBR (Balco et al., 2011).

The geomorphic model of PBR exhumation informed our sampling strategy, which involved collecting a vertical profile of ~7 samples down each PBR and pedestal (Supplementary Materials: Figure 1). By measuring the cosmogenic-nuclide concentrations at several heights on the PBR and pedestal, the forward model of Balco et al. (2011) was used to account for cosmogenic nuclide production occurring throughout the exhumation of the PBR from the subsurface. The method of Balco et al. (2011) models the ^{10}Be production before, during, and after exhumation of the PBR and finds the best fit of modeled nuclide concentrations to the measured nuclide concentrations for optimized values of the free parameters t_0, $\varepsilon_{0,sp}$, $\varepsilon_{0,mu}$ and ε_1. t_0 (years before present) is the time that the uppermost point on the PBR became exposed. $\varepsilon_{0,sp}$ and $\varepsilon_{0,mu}$ are effective erosion rates (m Myr^{-1}) used to specify depth-nuclide concentration profiles due to production by spallation and muon interactions, respectively, and therefore the initial nuclide concentrations in the samples at t_0. ε_1 is the exhumation rate of the PBR (m Myr^{-1}) during the subsequent period in which all the samples were exhumed. Best fit values of these parameters are used to determine the time t_{tip} (years before present), which is the time at which the lowest PBR-pedestal contact point became exposed and, therefore, the rock became fragile.

An important element of this forward model is that by parameterizing the initial conditions with separate effective erosion rates for production by spallation and muon interactions ($\varepsilon_{0,sp}$ and $\varepsilon_{0,mu}$) we avoid the necessity to assume a constant erosion rate prior to PBR exhumation. As our geomorphic model of PBR formation inherently involves a change in erosion rate at some unknown time before t_0, such an assumption of constant erosion would be inappropriate. The depth profile resulting from an unsteady erosion rate prior to t_0 is parameterized by a single effective erosion rate over the equilibration time of the production pathway (Bierman & Steig, 1996). This effective erosion rate may or may not be equal to the actual erosion rate at any particular time and is, therefore, not the instantaneous erosion at time t_0. The longer attenuation length of muons compared to spallogenic production results in a slower equilibration to a change in erosion rate and so $\varepsilon_{0,mu}$ is an apparent erosion rate over a longer timescale than $\varepsilon_{0,sp}$. Therefore, a given unsteady erosion history would imply that two different effective erosion rates are needed to separately parameterize nuclide concentration resulting from the two pathways. The forward model then assumes that at t_0 the entire PBR, from highest sample to lowest sample, is exhumed steadily at a fixed ε_1 rate. This steady state ε_1 erosion rate is appropriate given our geomorphic model of relatively short-lived, rapid saprolite erosion to exhume the corestone over the narrow height range (up to 2 m) of the sample locations.

In order to ensure that the model assumptions of Balco et al. (2011) were valid for each of the studied PBRs, we relied on field observations that would indicate the absence or occurrence of any post-exhumation erosion. For example, the observation of dark varnish on the surface of the PBR, its pedestal, and the surrounding outcrop would verify low post-exhumation erosion. In addition, planar sides of the PBR that align with joint planes in the surrounding outcrop would show that little post-exhumation erosion has changed the geometry of the PBR. Conversely, significant uniform physical weathering of the PBR, its pedestal, and surrounding outcrop could cause systematic errors in the model fitting of ^{10}Be concentrations to the measured values. In addition, evidence of post-exhumation physical weathering could cause the modeled ^{10}Be concentrations of individual samples to not match the measured ^{10}Be concentrations. An example of such post-exhumation physical weathering that would affect our modeling fitting is spalling of rock fragments caused by wildfires (Kendrick et al., 2016). The evidence of post-exhumation erosion would be on the ground surface at the base of the pedestal or apparent on the rock surface of the PBR itself. Qualitative field observations of both the absence and occurrence of post-exhumation erosion were used to determine our relative confidence in the fragility age modeling of each of PBR (see Supplementary Materials: Figure 1 for details about each studied PBR). A final model assumption is that there has been no reburial of the PBRs either during or after exhumation. The observations of PBR preservation in bedrock dominated landscapes with no fluvial fill terraces is evidence that eroded material is not being stored in the PBR catchments and, therefore, there is not the potential for eroded material to rebury the PBRs.

In this study, we implemented several changes to the model framework described by Balco et al. (2011). Our updated model can be accessed at *https://github.com/balcs/pbrs-2022*. Firstly, we set a limit on the parameters $\varepsilon_{0,sp}$ and $\varepsilon_{0,mu}$ to be within a factor of 2.5 of each other to prevent any geomorphically unrealistic solutions. This factor of 2.5 allows for the range of glacial (Last Glacial Maximum) to interglacial (modern) erosion rates (Marshall et al., 2017). Secondly, we updated the muon interaction cross sections to those of Balco (2017). Finally, to save computation time, we pre-calculated both production rates due to muons as a function of depth and muon-produced nuclide inventories as a function of $\varepsilon_{0,mu}$. These values are stored within a lookup table, which allows interpolation between values and speeds up the later Monte Carlo simulation because values do not have to be calculated for each iteration. The Monte Carlo simulations were run for all four free parameters ($\varepsilon_{0,sp}$, $\varepsilon_{0,mu}$, ε_1, and t_0) for 400 iterations. We investigated the initial Monte Carlo iteration as both the best-fit values of the free parameters as well as random values to ensure the optimization scheme always converged on a single minimum.

An important complexity in determining the fragility age of each rock is that the ^{10}Be production rate in each sample is not only modulated by the present-day complex outcrop geometry obstructing the cosmic ray flux to each sample point, but also by the varying thickness of overlying and surrounding regolith that lowers as the PBR is exhumed. Furthermore, the ~1-2 m height of the PBRs is similar to the characteristic e-folding length (distance to exponentially decrease by a factor of e, ~2.72) for cosmic ray-derived neurons at the Earth's surface, which means that, as it is exhumed, the PBR itself will partially obstruct the cosmic ray flux at most locations on the surface of the PBR or its pedestal. In order to quantify this shielding through time, 3-D models were constructed in *PhotoModeler* of each PBR, its pedestal, and adjacent outcrop. We then used both these 3-D models and the azimuth and elevation of the horizon topography measured in the field as inputs to the code of Balco (2014) to determine the sample specific parameters $S_{0,i}$ and L_i of Balco et al. (2011). $S_{0,i}$ and L_i describe the shielding factor at the location of each sample as a function of depth below the soil surface during various stages of exhumation.

^{10}Be sample preparation was conducted at Lawrence Livermore National Laboratory (LLNL), Scottish Universities Environmental Research Centre (SUERC), and the CosmIC laboratory at Imperial College London. The ~1 kg rock samples were crushed and sieved to collect 250–500 μm grains and purified to quartz mineral separates using magnetic separation and froth flotation, followed by acid etching to remove any atmospherically-derived ^{10}Be adhered to the grain surfaces (Kohl & Nishiizumi, 1992). During isotope dilution chemistry, Be was purified by anion and cation exchange and prepared into targets following the methodology of Corbett et al. (2016) for ^{10}Be/^{9}Be analysis by accelerator mass spectrometry (AMS).

Samples were measured by AMS at LLNL (Rood et al., 2010), SUERC (Xu et al., 2015), and the Australian Nuclear Science and Technology Organisation (ANSTO) (Wilcken et al., 2017) during the period of time from 2008 to 2019. The ^{10}Be/^{9}Be data from LLNL were normalized to the primary standard 07KNSTD3110 with an assumed value of 2.85×10^{-12}, the data from SUERC were normalized to National Institute of Standards and Technology (NIST) standard with an assumed value of 2.79×10^{-11}, and the data from ANSTO were normalized to the primary standard KN-5-2 with a nominal value of 8.558×10^{-12} (Nishiizumi et al., 2007). In all three AMS laboratories, two secondary standards were run as unknowns to confirm the linearity, accuracy, and precision of the measurements. The ^{10}Be/^{9}Be measured ratios were reduced to the number of total ^{10}Be atoms in each sample using the mass of low-background beryllium carrier added to each sample. A process blank, composed of the same mass of beryllium carrier only, was processed and measured with each batch of quartz samples. The ^{10}Be/^{9}Be measured ratios in each process blank were subtracted from every sample's ^{10}Be/^{9}Be measured ratios in that batch, and the 1σ AMS analytical errors for samples and associated blanks were propagated in quadrature.

To provide an important independent check on PBR exhumation rates ($\varepsilon_{0,sp}$, $\varepsilon_{0,mu}$, and ε_1) inferred from model fitting to samples on the PBRs, we calculated the erosion rate from 7 saprolite samples and 11 stream sediment samples at a subset of the PBR sites. These independent erosion rates, therefore, provided a quantitative test of the fragility age model that we used. These saprolite and stream sediment samples provided apparent steady state erosion rates over the integration time of ^{10}Be production. The unique temporal and spatial evolution of each PBR and its surrounding basin results in a unique combination of ε_0, ε_1, and present erosion rates in the independent apparent erosion rates. These erosion rate samples were prepared and analyzed following the same laboratory chemistry methods as the precariously balanced rock samples. Muon production parameters used for the erosion rate calculations are consistent with those used in our updated forward model for nuclide concentrations in PBR samples (Balco, 2017).

The saprolite samples were collected near the PBRs to test for a consistent erosion and exposure history of the granitic landscape surrounding and directly adjacent to each PBR. Each saprolite sample was either located at approximately the same elevation in the landscape as the PBR-pedestal contact or on the ground surface beneath the PBR sample vertical profile. A total shielding factor at the site of each saprolite sample was calculated as the product of the topographic shielding collected in the field and the shielding by the thickness of soil above the collected saprolite. The thickness of soil and thickness of collected saprolite sample were both also measured in the field. If consistent with the PBR samples, the ^{10}Be concentrations calculated in the saprolite sample should be similar to the range of ^{10}Be concentrations in the PBR samples closest in elevation to the saprolite sample. The calculated saprolite ^{10}Be concentrations are not necessarily expected to plot on the best-fit ^{10}Be modeled profile of the PBR due to differences in how the shielding is characterized between the two different sample types.

These ^{10}Be concentrations calculated for the saprolite samples were then used with version 3 of the online exposure age calculator described by Balco et al. (2008), and subsequently updated, to calculate the apparent steady state erosion rate and equivalent exposure age of each saprolite sample. The rate of ε_1, duration of ε_1, and how long before present ε_1 ended for each PBR will control how comparable the saprolite apparent erosion rate is to ε_1 and how comparable the equivalent exposure age is to t_{tip}. Similarly, the differences in shielding characterization between the saprolite and PBR samples requires that the saprolite calculated erosion rate and equivalent exposure age need only be broadly similar to the PBR data. A saprolite density of 2 g cm^{-3} was used. We used a constant production rate model and "St" scaling scheme for spallation (Lal, 1991; Stone, 2000), with a sea level high latitude reference ^{10}Be production rate of 4.132 ± 0.218 atoms g^{-1} yr^{-1} based on the "primary" calibration data set of Borchers et al. (2016).

The stream sediment samples were collected in the active channel downstream of the PBRs to obtain an average erosion rate of the granitic basin in which the PBR is located. The stream sediment erosion rates provide a more general test of our modeled PBR ε_0 and ε_1 erosion rates because the exhumation history at the location of the PBR is different from the surrounding drainage basin. This difference is due to the progressive conversion of the basin from a saprolite-mantled, low-relief landscape to a bedrock-dominated, high-relief landscape. Therefore, over the integration time of the stream sediment apparent erosion rate, different parts of the basin will have been in different disequilibrium states at different times. For that reason, in order to be consistent with the PBR model results the erosion rate calculated for the stream sediment samples needs only to be between the modeled values of ε_0 and ε_1.

The boundary of each basin draining to the sample point was delineated in ArcGIS (ESRI, 2020) from the 30 m SRTM dataset sourced from *OpenTopography* (https://opentopography.org) and the effective elevation, mean latitude, and mean longitude of each basin was determined for use in Version 3 of the online exposure age calculator described by Balco et al. (2008) and subsequently updated. Erosion rates were calculated using the same production rate and scaling scheme as for the saprolite samples. A sample thickness of 1 cm, and a sediment density of 2 g cm^{-3} were used as inputs for version 3 of the online exposure age calculator described by Balco et al. (2008) and subsequently updated.

PSHA Model

The PSHA model we validated with the PBR data was implemented using the open-source seismic hazard and risk calculation engine *OpenQuake* developed by the Global Earthquake Model (GEM) Foundation (Pagani et al., 2014). The *OpenQuake* engine provides tools, catalogs, and models to calculate and visualize earthquake hazard and risk, to which users can contribute enhancements for community driven development. These advantages have meant that the national seismic hazard models of seismically active countries such as Canada (Allen et al., 2020) and New Zealand (Abbott et al., 2020) have been translated into the *OpenQuake* engine as part of the worldwide coverage by *OpenQuake* and the GEM Global Hazard Mosaic.

The first necessary component of the PSHA model is a seismic source characterization. A seismic source characterization gives all possible earthquake ruptures and the probability of occurrence of each. The Third Uniform California Earthquake Rupture Forecast (UCERF3), developed by the U.S. Geological Survey and the Working Group on California Earthquake Probabilities, provides estimates of the magnitude, location, and time-averaged frequency of potentially damaging earthquakes across the state of California (Field et al., 2013). The UCERF3 seismic source model is used in the 2014 and 2018 updates of the U.S. Geological Survey National Seismic Hazard Model (USGS NSHM) (Petersen et al., 2014; Petersen et al., 2020). Epistemic uncertainty in the UCERF3 source characterization is included as alternative fault models, deformation models, and earthquake rate models, which are represented as seismic source characterization logic tree branches (Field et al., 2013).

In this study, the “true mean” UCERF3 model is used due to the complexity and computational intensity of the full UCERF3 model. This “true mean” model allows for the calculation of only one source model because the activity rate of each rupture is taken as the mean of the activity rates from all branches of the seismic source characterization logic tree in which the rupture appears. This “true mean” model is equivalent to the mean from the full seismic source characterization logic tree and was provided by Rao et al. (2017). However, the “true mean” model does not allow for the investigation of uncertainties in the seismic source characterization. Therefore, our study focuses exclusively on the validation of the ground motion characterization logic tree branches for the GMMs and their implications for hazard. Our results are, therefore, conditional on the assumption that the rates in the seismic source characterization are correct, however, in reality any inconsistencies between the PBR data and ground-motion estimates are likely due to a complex combination of both the GMMs and seismic source characterization.

The second necessary component of the PSHA model is a ground motion characterization (GMC). GMMs are used to express the intensity of a ground-motion parameter, e.g., PGA, in terms of the characteristics of the earthquake source, propagation path of the seismic waves, and the site conditions. In the past few decades, there has been a significant increase in the number of available GMMs as the quantity and quality of ground-motion recordings to constrain the models increase (Douglas & Edwards, 2016). However, each GMM invariably predicts different levels of average shaking than another GMM and so the use of multiple alternative models in PSHA creates epistemic uncertainty. The Pacific Earthquake Engineering Research Center (PEER) provides GMMs as part of the NGA-West2 project (Bozorgnia et al., 2014) that are used in the 2014 USGS NSHM (Petersen et al., 2014).

In both the USGS 2014 NSHM and this study, the referenced backbone GMM approach was used, where a central "backbone" GMM generalizes the attenuation behavior. Upper and lower alternatives about the central GMM are then defined to capture the epistemic uncertainty of a representative suite of published GMMs (Atkinson et al., 2014). The "backbone" method is advantageous for both regional and site-specific hazard analyses. At the regional scale of national seismic hazard maps, the "backbone" method allows a large number of possible GMMs to be represented by only a few alternatives, which reduces computational time. For site-specific-seismic hazard analyses, the "backbone" method more accurately captures the epistemic uncertainty because the alternative, conventional method of using simple weighted combinations of available GMMs is inadequate to capture the epistemic uncertainty.

The GMMs require input parameters that characterize the site response at the location of interest. For each of the PBR sites, the average seismic shear-wave velocity in the upper 30 m, the V_{S30} value, was interpreted from the map of Thompson et al. (2014). Z1.0 value, the depth at which shear wave velocities reach 1 km/s, were calculated using the equation of Chiou and Youngs (2014). Z2.5 value, the depth at which shear wave velocities reach 2.5 km/s, were calculated using the equation of Campbell and Bozorgnia (2008). Importantly, Stirling et al. (2002) showed that there was no evidence of anomalous site conditions at PBR sites in southern California, which showed that the preservation of PBRs where large ground motions are estimated to occur cannot be explained by anomalous site conditions.

The 2014 USGS NSHM (Petersen et al., 2014) uses five GMMs: ASK14 (Abrahamson et al., 2014), BSSA14 (Boore et al., 2014), CB14 (Campbell & Bozorgnia, 2014), CY14 (Chiou & Youngs, 2014) and I14 (Idriss, 2014). These five GMMs were derived from the PEER NGA-West2 ground-motion recording database (Bozorgnia et al., 2014). The 2018 USGS NSHM (Petersen et al., 2020) uses four of these five GMMs. The epistemic uncertainty of the upper and lower alternatives about each central GMM were defined based on the number of earthquake recordings in each magnitude-distance bin used in the modeling (Petersen et al., 2014). We use all five NGA-West2 GMMs with the same ground motion characterization logic tree and GMM branch weights as the USGS 2014 NSHM. The five GMMs and three alternatives of each GMM result in 15 logic tree end-branch hazard curves for each PBR site, each of which we validate in turn. These end-branch hazard curves and their weights are also used to calculate a mean hazard curve for each PBR site.

The NGA-West2 GMMs employ the ergodic assumption, where the distribution of ground motions over time at the site of interest is treated the same as the spatial distribution over all sites globally (Anderson & Brune, 1999). The GMM median estimate and variance are, therefore, derived from instrumental recordings from a global database of different seismic sources and sites, not just the seismic source and site of interest. The ergodic assumption is necessary due to the unlikely recording of a historical earthquake at the site of interest, as well as the limited number of instrumental recordings of rare, large earthquakes that are needed to constrain site- and source-specific effects.

While the PBR independent data do not provide a direct constraint on the GMMs at the PBR site, the PBRs do provide constraints on the hazard curves, which indirectly provide constraints on the GMMs because the uncertainty in the GMMs tends to dominate the uncertainty in the hazard curves for long return periods (Anderson & Brune, 1999). Therefore, our PSHA model, which includes the published NGA-West2 GMMs, does not allow the investigation of what specific issue with a GMM may be the cause of any inconsistency with the PBR validation data. Our model also does not allow us to explore the appropriate modifications to the GMMs that would make the ground-motion estimates at long return periods more consistent with the PBR validation data, such as an appropriate physical limit or the appropriate number of standard deviations to truncate the estimates (Bommer et al., 2004). We can only conclude that there is some issue with the application of these ergodic GMMs to accurately describe the source, path, and site of the PBRs. However, the independent observational PBR data allow the validation of each published form of the NGA-West2 GMMs, which can be used as part of the selection criteria for the suitable suite of GMMs to include in the PSHA model for a site.

Hazard Model Validation

We followed the methods of Rood et al. (2020) and individually validated each logic tree end-branch hazard curve output from the PSHA model. We used each PBR to validate the ground motions estimated for the site of that PBR. At each individual PBR site, the validated hazard curve was rejected as inconsistent with the PBR data if the probability of survival of the PBR over the fragility age of the PBR was less than 5%. Moreover, because all 20 PBR sites have identical ground motion characterization logic trees, we, therefore, validated each ground motion characterization logic tree GMM end-branch 20 times, which then allowed us to investigate the relative frequency with which each GMM is inconsistent with PBR data across southern California.

We executed our PSHA model to calculate hazard estimates for scalar ground motions that depended only on PGA, and our PBR fragility functions are based on PGA; therefore, the hazard curves and PBR fragility functions are directly comparable. First, for each output PGA hazard curve, the rate of occurrence of PGA is obtained as the derivative of the hazard curve annual frequency of exceedance.

Second, the rate of failure for the PBR is obtained by multiplying the PBR probability of failure for a given level of PGA with the rate of occurrence of that level of PGA and then summing these combinations for all levels of PGA (Equation 1). The rate of failure of the PBR was then used to calculate its probability of survival over median fragility age of a PBR (T) (Equation 2). We identified the individual PSHA hazard curves for which there is a greater than 95% probability of PBR failure (less than 5% probability of survival) following the methods of Rood et al. (2020).

$$\gamma_{Failure} = \int P(Failure|PGA = a).\left|\frac{\partial\gamma(a)}{\partial a}\right|\partial a \qquad (1)$$

$$P_{survival} = e^{-\gamma_{Failure}T} \qquad (2)$$

RESULTS

For brevity, we present the detailed results and associated summary figures of a representative PBR, GV2, in the main text, and provide the figures and data tables for each of the remaining PBRs in the Supplementary Materials.

PBR Fragility

The detailed 3-D model of the PBR GV2 can be seen in Figure 2A, from which the geometric parameters α and R are measured in Figure 2B. These measured geometric parameters and calculated p^2 values for all 20 PBRs are provided in Table 2. The α values in the most fragile direction, α_1, which is the direction the PBR will topple, range from 0.16 to 0.50 radians for the 20 PBRs. PBRs with lower α values are more fragile and PBRs with higher α values are more stable. Based on these α values alone, a simple assessment of relative fragility suggests that MR1 is the most fragile PBR that we studied, and BS1is the most stable. LJ5 is the only studied PBR that possesses a symmetric geometry and thus symmetric rocking response to earthquake ground shaking. The observed predominance of asymmetric PBRs highlights the importance of considering not only the direction the PBR will topple but also the conjugate rocking direction. The most asymmetric rock is LJB2, for which α_2 is 3.7 times greater than α_1. This large asymmetry will greatly dampen the rocking response of LJB2, despite appearing to be one of the most fragile studied PBRs, if only considering the α_1 value (Table 2).

Seven of the studied PBRs possess α_2 values that are greater than the range investigated and parameterized by Purvance et al. (2008a); therefore, we set the α_2 values of these PBRs to 0.5 radians in our fragility calculations. The use of the assigned 0.5 value, as opposed to the measured α_2 values of these PBRs, does not produce a significant difference in the fragility of each PBR. The greater the degree of asymmetry in the geometry of the rock, the greater the degree of dampening of the rocking response, which, in turn, makes the PBR more stable. An increase in either PGA or PGV/PGA always results in an increase in the probability of toppling of a PBR. The mean magnitude and distance results for all 20 PBR sites that were used to calculate the conditional distribution of PGV/PGA for each investigated PGA value are provided in Table 2. The PGA-based fragility function for the PBR GV2 is shown in Figure 2C.

PBR Fragility Age

The following PBR fragility age results are informed by an exceptionally large dataset of ^{10}Be AMS analyses (175 total: 134 PBR samples, 23 process blanks, 11 stream sediment samples and 7 saprolite samples). All the information necessary to calculate the ^{10}Be concentrations and 1σ uncertainties from the measured ^{10}Be/^{9}Be ratios are provided in Supplementary Materials: Table 1.

The position of the samples collected from all 20 PBRs for cosmogenic-nuclide surface exposure dating are displayed in Figure 3. The position of these samples, the PBR, the pedestal, and the surrounding outcrop were all incorporated into a 3-D model. The 3-D models were used to calculate the sample specific shielding constants $S_{0,i}$ and L_i, which are given for GV2 in Table 3. For GV2, the samples show the general trend of decreasing $S_{0,i}$ and increasing L_i as the distance of the sample from the top of the PBR increases. The cosmogenic ^{10}Be concentrations and 1σ uncertainties calculated for each GV2 sample are also given in Table 3. The expected general decrease in ^{10}Be concentrations with increasing sample depth, i.e., distance below the top of the PBR, can be clearly observed. The corresponding data to Table 3 for the other studied PBRs is provided in Supplementary Materials: Table 2.

The data in Table 3 and Table S2 were used as the input to the fragility age forward model to calculate the age of fragility, t_{tip}. For all 20 PBRs, the best fit values of the parameters $\varepsilon_{0,sp}$, $\varepsilon_{0,mu}$, ε_1, and t_0 predict ^{10}Be concentrations that are in good agreement with the measured concentrations and 1σ uncertainties, as can be seen in Figure 3 and Supplementary Materials: Table 3. The model predicted ^{10}Be concentrations are attributed to the 3 phases of PBR exhumation: before exhumation, during exhumation, and after exhumation. The ^{10}Be concentration accumulated in each sample before PBR exhumation always follows an exponential decrease with sample depth because of the attenuation of the cosmic rays. The ^{10}Be concentration accumulated in each sample after PBR exhumation is modulated by the modern shielding factor, $S_{0,i}$, of each sample. We selected the median value of the 400 Monte Carlo simulation as our preferred value for each parameter, and used the 16th and 84th percentile values to capture the uncertainty on the median value (Figure 3 and Supplementary Materials: Table 4). Notably, for all 20 PBRs, the best fit value of each parameter overlaps within 16-84th percentile uncertainties of the Monte Carlo simulations, as is shown in Table 4 for GV2. Furthermore, our recalculated fragility age of the PBR GV2, the case study PBR in Balco et al. (2011, 2012), is in agreement with the age calculated by Balco et al. (2012): 17.6 ka (16.5 – 18.8 ka 16th-84th percentile uncertainty) compared to 18.5±2.0 ka, respectively. This agreement between ages shows that the parameter updates we made in the model only have a small effect on the results.

The fragility ages of the 20 studied PBRs range from approximately 1.5 ka to 50 ka. Therefore, it is clear that no singular climate-driven pulse of erosion caused exhumation at all places on the landscape at the same time to simultaneously form all the PBRs in southern California (Figure 4). In fact, half of the PBRs (10 out of the 20) have fragility ages younger than 10 ka. Therefore, assuming a ubiquitous minimum fragility age of 10 ka, as has been previously done (Grant Ludwig et al., 2015), would overestimate the age of half the studied PBRs. Our results show that the fragility age of any given PBR is modulated by its unique position in the landscape. The three PBRs with the youngest ages, i.e., less than 2 ka, are the three studied PBRs geomorphically located within an ephemeral fluvial channel. The oldest PBR is LJ5, which has a fragility age of 49.8 ka (48.3–51.2 ka 16^{th}-84^{th} uncertainty). LJ5 is elevated above an ephemeral fluvial channel and has well-developed dark varnish, which is consistent with old age. Importantly, this age for LJ5 is significantly older than any previously dated PBR in southern California; therefore, it is logical that some PBRs have survived for significantly longer than previously thought.

The modeled ε_0 and ε_1 erosion rate results validate our geomorphic model for PBR formation in which an initially low rate of subsurface weathering (i.e., $\varepsilon_{0,sp}$ and $\varepsilon_{0,mu}$) is followed by an increased rate of erosion during exhumation (i.e., ε_1). The modeled ε_1 erosion rates during PBR and pedestal exhumation range over several orders of magnitude, i.e., less than 100 m/Myr to 10,000 m/Myr. Therefore, pedestal height cannot be used as a proxy for relative PBR age, which is contrary to previous ideas based on anecdotal evidence. It is important to note that modeled ε_1 erosion rates of 10,000 m/Myr reveal that the contribution of production during exhumation of the PBR to the total nuclide concentration is at or below the noise level. Therefore, a modeled ε_1 erosion rate of 10,000 m/Myr should not be interpretated as an estimate of the absolute exhumation erosion rate, but instead that the exhumation of a PBR was instantaneous within the resolution of the model.

The PBR forming erosion rates broadly fall into three categories: 1) low ε_0 and increased but still low ε_1, 2) low ε_0 and instantaneous ε_1, and 3) high ε_0 and low ε_1 (Figure 5). The erosion rates of the two PBRs in category 3 (PC1 and PP1; Figure 5) appear inconsistent with our geomorphic model of PBR formation. However, we suggest that the apparent instantaneous ε_0 values of the category 3 PBRs indicate that the ε_0 signal has been completely removed from these landscapes by ε_1 and so ε_0 is an unconstrained parameter for these two PBRs. This ε_0 signal removal would be caused by a longer-lived ε_1 period and, therefore, a greater thickness of saprolite layer eroded at the location of these two PBRs. In this case, our geomorphic model remains valid, but the rate of the low erosion subsurface weathering phase is not possible to constrain by our fragility age model for these two PBRs. Alternatively, these apparent instantaneous ε_0 values may be due to post-exhumation erosion of these PBRs, which is substantiated by field observations of anomalously intense chemical and physical weathering on these category 3 PBRs (Figure 3; Supplementary Materials: Figure 1). Because such post-exhumation erosion would violate the assumptions of our geomorphic model, we therefore have low confidence in the fragility age modeling results for these two PBRs (PC1 and PP1).

The erosion rates calculated from the stream sediment and saprolite samples are consistent with the PBR ε_0 and ε_1 erosion rates. Without exception, in agreement with our geomorphic model, the stream sediment and saprolite erosion rates at each site are between ε_0 and ε_1 of the PBR(s) at that site (Figure 5). For example, the GV2 stream sediment erosion rate of 85.5±5.7 m/Myr and saprolite erosion rate of 82.2±5.4 m/Myr overlap within uncertainties. These erosion rates fall between the median ε_1 erosion rate of 206.8 m/Myr (158.8-330.4 16^{th}-84^{th} percentile) than the median $\varepsilon_{0,sp}$ rate of 15.9 m/Myr (14.8-17.1 16^{th}-84^{th} percentile), which indicates that the erosional signature of the local landscape has evolved from ε_0 towards ε_1. In the cases where the modeled ε_1 erosion rates are instantaneous, the sediment and saprolite erosion rates show that the local landscape has evolved towards a higher erosion rate than ε_0, which includes periods of rapid erosion over the lengthscales of the height of PBRs (1-2m). The consistency of these modeled and observed PBR-forming erosion rates, therefore, supports our fragility age methods and associated results. All the inputs necessary to calculate the stream sediment and saprolite erosion rates are provided in Supplementary Materials: Tables 4 and 5, respectively.

Furthermore, the ^{10}Be concentrations in the saprolite samples are consistent with the range of ^{10}Be concentrations in the PBR samples closest in height to the saprolite sample (Figure 3). Erosion rates calculated from the saprolite samples that are lower than ε_1 indcate that the rapid ε_1 erosion rate reached the modern saprolite surface before the present time and that ^{10}Be surface production with negligible erosion has been occurring since that time. The two simplest case PBRs to illustrate this point are PNT01 and SW02, because all ^{10}Be accumulated in the saprolite samples was produced during post-ε_1 exposure due to their instantaneous ε_1 values. We calculated 8193±300 year and 937±80 year exposure ages for the PNT01 and SW02 saprolite samples respectively, assuming zero erosion and no inheritance (Supplementary Materials: Table 6). These two saprolite exposure ages overlap within the uncertainties on the t_{tip} ages of PNT01 and SW02. This agreement in ages further validates our geomorphic model that the rapid saprolite erosion to exhume the PBR, ε_1, abruptly stopped at the present ground surface level, and since that time has been accumulating ^{10}Be at a negligible erosion rate.

PSHA model

The *OpenQuake* engine outputs 15 alternative ground-motion estimates as hazard curves from our PSHA model, one for each of the ground motion characterization logic tree 15 GMM end branches. Therefore, 15 alternative hazard curves were calculated for the location of each of the 20 PBRs. The 15 output hazard curves for GV2, as well as the weighted mean, are presented in Figure 6A. The hazard curves of each GMM have a unique shape attributed to the differences in earthquake recording selection criteria as well as the subsequent model development of predictor variables. The epistemic uncertainty among the GMMs results in a large width of hazard curve distribution. The spread in the hazard curves in Figure 6A shows that the five GMMs compare more favorably for the short return periods with differences becoming more significant at longer return periods. Equivalent figures for all the PBRs are included in the Supplementary Materials: Figure 1.

Hazard Model Validation

We validated, in turn, each of the 15 end-branch hazard curves output from each PBR site PSHA model using the combination of the fragility function and median fragility age of each PBR. The ground-motion estimates and associated GMM logic-tree branch are categorized as inconsistent with the survival of the PBR if there is a less than 5% probability of survival of the PBR with that ground-motion estimate. Intuitively, it is the hazard curves that estimate the highest ground motions at the lower annual frequencies of exceedance, for example the upper GMM branches relative to the central GMM branches, that are inconsistent with the PBR survival. The fragility and fragility age of GV2 is consistent with only 9 out of 15 of the output ground-motion estimates: the central and lower alternatives of ASK14, BSSA14, CB14, and CY14 and only the lower alternative of I14 (Figure 6C, Table 5). Therefore, the upper alternatives of all five GMMs and the central alternative of I14 are rejected on the basis of inconsistency with the unexceeded ground motions recorded by GV2.

In our regional analysis, no GMM ground-motion estimates are consistent with all of the PBRs (Table 5). In fact, one of the studied PBRs, BR1, was not consistent with any of the 15 output hazard curves for this site. The PBRs BS1, LJ1, PI2, and SW02 were the only PBRs consistent with all ground motion characterization logic tree GMM end branches. For example, the PBR SW02 has a fragility function median of 1.31 g and is the least fragile of the youngest three PBRs that all have a fragility age of <2 ka. Notably, BS1 was the least fragile of our studied PBRs, with a fragility function median of 3.69 g. Furthermore, the PBR SW02 has a fragility function median of 1.31 g and is the least fragile of the youngest three PBRs that all have a fragility age of <2 ka. These cases illustrate the equal necessity of accurately determining both the fragility and fragility age of a PBR in order to determine how informative a PBR will be in constraining ground-motion estimates.

The GMM I14 is the most frequently inconsistent with the PBR empirical data. Not only are the central-I14 ground-motion estimates inconsistent with 14 of the 20 PBRs, but also the upper-I14 ground-motion estimates are inconsistent with 16 of the 20 PBRs. The frequency of rejection of the GMM I14 provides the basis that is invalidated by our empirical PBR data, which, in turn, provides a reasonable justification to remove I14 from the PSHA model. Next, we investigated the improvement to the ground-motion estimates that could be made by removing the GMM I14 from the ground motion characterization logic tree. We set the weight of the I14 branch to zero and then renormalized the weights of the remaining four GMM branches at this node in the ground motion characterization logic tree to again sum to one. At the annual frequency of exceedance corresponding to a 2% probability of exceedance in 50 years, the 2475 year mean return period relevant for national seismic safety regulations and building code design standards, the removal of I14 reduced the mean ground-motion estimate by 2-7% at our PBR sites. More importantly, the removal of the invalid I14 GMM from the PSHA model significantly reduced the ground motion uncertainty range for the 5th–95th fractiles by 10-36% at our PBR sites.

DISCUSSION

The validation of PSHA output ground-motion estimates, and, in turn, the alternative GMM input parameters, offers a unique opportunity to reduce uncertainties in ground-motion estimates of rare, large earthquakes. The rejection and reconsideration, or removal, of PSHA input parameters, e.g., GMMs as investigated here, provide the opportunity to assess the sources of epistemic uncertainty in the PSHA model. Importantly, the independent PBR empirical data provides ground-motion information over timescales longer than historical earthquake recordings: timescales where ground-motion estimates are extrapolated but unvalidated until now. In this section, we discuss the assumptions and limitations of our methods as well as the implications and applications of our results.

PBR Fragility

The most fragile 2-D rocking geometry when doing probabilistic PBR fragility analyses using the equations of Purvance et al. (2008a) has neither been previously reported nor its significance systematically investigated. We identified two alternative methods of selecting the two critical PBR rocking points: 1) the rock's minimum α rocking point and corresponding α_2 rocking point 180 degrees through the center of mass, and 2) the α_1 and α_2 rocking points that produce the narrowest base through the center of mass. In the case of a 3-D rectangular block, which was the geometry originally investigated by Purvance et al. (2008a), these two alternative methods produce the same critical rocking points. However, for more complicated PBRs geometries, such as those investigated here, these two alternative methods often produce different critical rocking points.

To compare the alternative methods, we calculated the median of the fragility function of each PBR using the α_1 and α_2 angles determined by each of the two alternative critical rocking point estimation methods. There was only a greater than 5% difference in the calculated median fragility for one of the PBRs. This PBR, BS2, has a tapering wedge geometry, resulting in a ~20% difference in $\alpha_1$values and ~50% difference in α_2 values between the two methods. We believe these differences show that the geometry of this rock is too dissimilar from the rectangular block geometry that the Purvance et al. (2008a) fragility equations were intended to model, and reinforces the value of modeling in 3-D the rocking response of each PBR (Veeraraghavan et al., 2017). We, therefore, have low confidence in the fragility results for PBR BS2. A qualitative assessment of how well the toppling equations of Purvance et al. (2008a) model each PBR can be made from how similar the geometry of the PBR-pedestal contact is to that of a rectangular block (Figure 2B; Supplementary Materials: Figure 1). Importantly, the majority of the studied PBRs have geometries that approximate a rectangular block and, therefore, the selected critical rocking points are identical in both alternative methods. However, when the critical rocking points are not identical between the two methods, the critical rocking point estimation method based on the narrowest base will always yield a larger α_1 value, which is the primary variable in the fragility of the PBR when using the Purvance et al. (2008a) equations.

Therefore, our use of the critical rocking points for the narrowest base results in larger α_1 value and, therefore, a less fragile geometry being used for each PBR.

It is desirable for precariously balanced rocks to be located at short distances (e.g., <10 km) from local seismic sources in order to place the greatest constraints on ground-motion estimates. These are distances at which there is a directionality to the earthquake ground motions, and the direction of maximum ground motion may or may not differ from the orientation of the PBR α_1 direction. However, Veeraraghavan et al. (2017) showed that the complex geometry of the PBR-pedestal contact means that PBR rocking could be initiated by a maximum ground motion applied in any direction, but that the rock will still most likely topple in the vicinity of the α_1 direction, regardless of the direction of the initial ground motion. Furthermore, Veeraraghavan et al. (2017) also showed that the 2-D rocking geometry of Purvance et al. (2008a) generally underestimates the rocking response compared to that of its 3-D dynamic rocking geometry; therefore, the 2-D geometry is a lower estimate of the PBR's fragility, and the 3-D geometry may be more fragile. Therefore, our fragility estimates are likely a minimum fragility for the rocks because of our choice of critical rocking points and 2-D geometry.

In our study, we assigned the PBRs a constant fragility and fixed rocking points during the duration of time from their fragility age (t_{tip}) to the present. This assignment was based on our geomorphic model of granitic corestone PBR formation, our definition of fragility age, and our assumption and supporting field observations of negligible post-exhumation erosion. Baker et al. (2013) and Hanks et al. (2013) considered conceptual models of fragility evolution and the associated constraints on hazard estimates. However, the evolution of the fragility of a PBR is dependent on the unique post-exhumation history of each PBR. In theory, whether the post-exhumation erosion occurs predominantly at the top or bottom of a PBR will dictate whether a PBR evolves to a more stable or more fragile geometry with time. For example, on one hand, erosion at the top would reduce the PBR height through time and lower the center of mass, which would make the PBR more stable. On the other hand, erosion predominantly at the base of a PBR would reduce the PBR basal area, raise the center of mass, and narrow the distance between the rocking point and center of mass, which would make the PBR more fragile. In the absence of any information about the post-exhumation erosion history of each PBR, it is not possible to model a time-evolving fragility. With this limitation in mind, we attempted to focus our studies on PBRs where field evidence supported the absence of post-exhumation erosion. Therefore, we believe that the assumption of a constant fragility is reasonable and justified.

PBR Fragility Age

Our method of measuring cosmogenic-nuclide concentrations in a vertical profile down the PBR and pedestal allows us to model cosmogenic nuclide production occurring throughout the exhumation of the corestone PBR from the subsurface. However, the PBRs we studied that did not have all the samples in a single vertical profile, e.g., GV1, resulted in non-systematic shielding with depth below the top of the PBR ($S_{0,i}$ and L_i), which was found to be advantageous. It can be seen in the Supplementary Materials: Figure 1 that the present-day shielding of the sample GV1-1 resulted in the post-exhumation ^{10}Be depth concentration profile to be distinct from the pre-exhumation ^{10}Be depth concentration profile. Conversely, when the sampled side of a PBR was a simple planar surface, the ^{10}Be profile accumulated after exhumation could resemble the ^{10}Be profile accumulated before exhumation. This has the potential to result in a non-unique solution of modeled nuclide concentrations to the measured nuclide concentrations. Therefore, in future PBR fragility age investigations, we advise that, in addition to collecting a vertical profile of samples, a minimum of a single sample should be collected from a location on the PBR that will have a distinct shielding value from the samples in the vertical profile.

The majority of the fragility age modeling results show an approximately normally distributed histogram of Monte Carlo simulation t_{tip} results (Figure 3). Six of the studied PBRs (BS2, LB05, MR1, SW02, UCR1, and YV1) have an additional young (i.e., t_{tip} ~ 0 ka) histogram peak and/or tail in the fragility age results. However, the t_{tip} median values of these six PBRs are still in good agreement with the best fit t_{tip} values, and the best fit values fall well within the 16th-84th percentile confidence intervals. Importantly, the effect of the young t_{tip} peaks and/or tail will always be a younger median t_{tip} value, which results in a lesser constraint to the ground-motion estimates. These six PBRs include the three youngest PBRs, all of which are in similar geomorphic locations within an ephemeral stream channel. These results suggest that PBRs within active stream channels have a high probability of being the most recently exhumed and therefore have the youngest fragility ages. Therefore, we suggest that in future studies PBRs located in a stream channel are not selected for investigation because not only do younger t_{tip} values provide less constraint on the hazard estimates but also the younger t_{tip} values are not as well constrained by our fragility age model.

The PBR LJB2 has Monte Carlo t_{tip} results that do not generate a well-defined t_{tip} histogram peak, but instead generate a spread of t_{tip} ages from ~2 ka to ~22 ka. The histogram shows a general increase in frequency towards the older t_{tip} ages with the highest frequency bar at ~20 ka. It could, therefore, be proposed that a fragility age of <20 ka is the best estimate that can be made from the Monte Carlo results for this PBR. Conversely, the median t_{tip} value and best estimate value are in good agreement and are younger than a <20 ka age, so result in a lower constraint on the ground-motion estimates. We selected to use the median t_{tip} value of LJB2 in our analysis to be consistent with the fragility ages of the other PBRs. It is interesting to note that the three shortest studied PBRs, all with heights under 1 m, are BS2, LJB2, and UCR1, which all had similar non-standard t_{tip} modeling results. We suggest that both the reduced height over which to model the ^{10}Be data and the reduced range of shielding factors due to the reduced distance between samples resulted in non-unique solutions and, therefore, the lack of a clear t_{tip} histogram peak. Despite our assumption of linear exhumation being more likely to be correct over shorter PBR heights, such ambiguous model results give us only moderate confidence in the fragility ages for LJB2, BS2, and UCR1.

If our studied PBRs were in a landscape with steady state erosion, our fragility age model results would be $\varepsilon_0 = \varepsilon_1$. Conversely, the observed dissimilar values of ε_0 and ε_1 are evidence of an unsteady erosional history and support our separate modeling of $\varepsilon_{0,sp}$, $\varepsilon_{0,mu}$, and ε_1 apparent erosion rates. The fact that there is still an ε_0 signal retained within the PBR samples means that ε_1 was short-lived and eroded a saprolite layer of finite thickness before transitioning to the present bedrock-dominated low erosion landscape. Nearly all of our PBR modeling results show $\varepsilon_0 < \varepsilon_1$, which is in agreement with our geomorphic model of PBR formation. Conversely, the theoretical random sampling of landscape erosion rates would be expected to yield $\varepsilon_0 < \varepsilon_1$ as often as $\varepsilon_0 > \varepsilon_1$. Although there are two cases, PC1 and PP1, where the model predicts $\varepsilon_0 > \varepsilon_1$ that do not match our geomorphic model of PBR formation, these two cases do verify that our fragility age model is functioning correctly because it can and will yield such results. In summary, our set of modeled ε_0 and ε_1 erosion rates agree with the independent geomorphic observations and interpretations of the landscape evolution at the PBR sites.

The independent saprolite and stream sediment samples are an important test of whether the PBR fragility age modeling results are consistent with landscape-forming processes. The saprolite and stream sediment erosion rates we calculated for the PBR sites are not only consistent with our PBR modeled PBR erosion rates, but are also consistent with the erosion rates previously calculated in the San Bernadino Mountains by Binnie et al. (2007) and the San Gabriel Mountains by DiBiase et al. (2010). The area of the PBR catchments of ~0.5 – 5 km^2 is within, but at the low end of the range of catchment areas studied by Binnie et al. (2007) and DiBiase et al. (2010). However, our range of calculated saprolite erosion rates (34 - 892 m/Ma) and sediment erosion rates (30 – 174 m/Ma) is in good agreement with the range of 35 – 1100 m/Ma calculated by DiBiase et al. (2010). The consistency between our modeled erosion rates with that of other regional datasets give us confidence that our forward model accurately captures regional erosional processes, which, in turn, gives us confidence in our fragility ages.

PSHA Model

In our analysis, we used the published GMM standard deviations as the aleatory variability, which, therefore, includes site-to-site variability in the inter-event and intra-event variability. We decided to use the NGA-West2 GMMs as used in the 2014 USGS NSHM project (Petersen et al., 2014) and so did not conduct a site-specific analysis for the location of each PBR to determine non-ergodic site terms. A site-specific analysis would have had the effect of trading aleatory variability for epistemic uncertainty and allowed the ground motion characterization logic tree branches for each GMM site term to be validated. Our validation results of the GMMs do not account for appropriateness of the site terms and with our use of the full aleatory variability. Therefore, it is possible that a GMM may have passed the PBR validation if a site-specific analysis had been conducted and the site-specific terms used in the GMM. It was beyond the scope of our study to conduct such site-specific analyses for all 20 PBR sites, but we suggest they be incorporated into future PBR hazard validation studies.

Hazard Model Validation

Of the five NGA-West2 GMMs, the model I14 was derived from the fewest empirical ground-motion recordings and is applicable over the narrowest magnitude and distance range (Gregor et al., 2014). The frequency of rejection of I14 by our empirical PBR data, relative to the other NGA-West2 GMMs, we believe demonstrates the inherent limitation of GMMs extrapolated to ground motions beyond the empirical recordings from which they are derived. In order for GMMs to perform well at these extrapolated ground motions, we show that more constraining data are essential. One suggestion, to maximize the number of ground-motion recordings used by all GMMs, would be the adoption of Bayesian updating of GMMs to incrementally update each model as new ground-motion recordings become available (Stafford, 2018). Therefore, the long wait between updates and revisions to existing models, such as from NGA-West1 in 2008 to NGA-West2 in 2014, would be avoided. However, it is important to note that this will not contribute to the improvement of the GMM estimates at the timescales of thousands to tens of thousands of years, which are validated by the PBRs.

In addition, I14 is the simplest of the NGA-West2 GMMs in that its form contains the fewest predictor variables. I14 is the only NGA-West2 model not to define normal faulting as a style of event, nor provide any regional adjustment (Gregor et al., 2014). Additionally, I14 does not include non-linear site response, nor finite fault effects (Idriss, 2014). We suggest that frequency of rejection of I14 by our empirical PBR data, relative to the other NGA-West2 GMMs, also demonstrates the inherent issues with the ergodic assumption in PSHA, and specifically GMMs. The shape of the ergodic hazard curves at the low frequencies of exceedance uniquely tested by the PBR data are highly sensitive to the variability about the GMM median at a high number of standard deviations, which we show are inconsistent with our PBR data. The lessened extent to which the model I14 associates both recorded and, therefore, estimated ground-motion levels to the unique location-specific source, path, and site variables results in the higher rejection rate of ground-motion estimates by our PBR data.

In this study, our objective was to validate each of the five published NGA-West2 GMMs, which were the suite of GMMs selected for use in the 2014 USGS NSHM (Petersen et al., 2014). However, if we were to have used the GMM selection criteria of Bommer et al. (2010), we suggest that the model I14 would be excluded from use based on the method of regression analysis to derive the model. In fact, of the five NGA-West2 GMMs, the model I14 is infrequently selected in engineering projects. Therefore, we suggest that our findings provide empirical evidence of the importance of using such GMM selection criteria in eliminating candidate GMMs models from use in analysis. Interestingly, in the model update from the 2014 USGS NSHM to the 2018 USGS NSHM, the GMM

I14, the GMM that we identified as most frequently inconsistent with our PBR data, was no longer included. This decision to no longer include I14 in the 2018 USGS NSHM was because I14 can only be applied for soil site conditions with V_{S30} from 450 to 2000 m/s, whereas applications for soil site conditions with V_{S30} down to 150 m/s are necessary for updated building code requirements (Petersen et al., 2020). While this decision to no longer include I14 was based on the output requirements and applications of the end users, our PBR validation results independently support this decision. In fact, we suggest that the inconsistency of I14 with our empirical PBR data provides another criteria to no longer include this GMM in future hazard models in California. Furthermore, our methods can be applied to validate and select any GMMs for any PSHA model, not only the NGA-West2 GMMs.

It is important to recall that any conclusions we make about the validity of the GMMs is conditional on the assumption that source model rates are correct. We combine the upper, central, and lower alternative of each GMM with the "true mean" UCERF3 seismic source characterization for southern California. Therefore, the rejection of the "true mean" UCERF3 model and central GMM by a significant subset of the PBR data indicates that the inconsistencies that we observed between the ground-motion estimates and the unexceeded ground-motions derived from PBR data cannot be explained by solely investigating the epistemic uncertainty of the GMMs. Instead, this suggest that some component of the inconsistency is originating in the "true mean" UCERF3 seismic source characterization. In addition, it is important to remember that each PBR provides a site-specific validation of the relative performance of all five of the NGA-West2 GMMs. Therefore, our results only invalidate a particular GMM at our PBR sites in southern California, whereas at other sites globally that GMM may be appropriate to include in the hazard model.

It can be seen in Figure 1 that the seven PBRs for which all the ground-motion estimates are inconsistent with the PBR data are spatially distributed across southern California. The dominant seismic sources at the sites of the PBRs BR1, RT1, and PP1 are the San Jacinto and Elsinore faults. At LB05, LJB1 and LJB2 the dominant seismic source is the Mojave section of the San Andreas fault. At PNT01 the dominant seismic source is the Pinto Mountain fault. Therefore, our results do not suggest that the mischaracterization of a particular fault in the UCERF3 seismic source characterization is responsible, but instead suggest the parameter models within the seismic source characterization require further investigation to deconvolve from where the inconsistencies with the PBR data are arising. Therefore, future PBR validation could consider the complete combination of the full seismic source characterization logic tree with the ground motion characterization logic tree. This future research would also have the advantage of investigating which alternative parameter models and values in the seismic source characterization are producing the inconsistent ground-motion estimates.

Until now, there was no method to empirically test the resultant ground-motion estimates of these GMMs at the timescale of rare, large earthquakes. Our study provides a novel tool to reduce the epistemic uncertainty in the ground-motion estimates by the rejection and subsequent removal of GMMs from the PSHA model seismic source characterization because their ground-motion estimates are inconsistent with and, therefore, invalidated by independent precariously balanced rock data. On the one hand, from a scientific perspective, the validation of each of the individual PSHA output earthquake ground-motion estimates permit the understanding of which parameters in the PSHA model are inconsistent and so require redevelopment of our understanding. On the other hand, from an engineering perspective, as the worst-case ground-shaking scenarios are rejected and removed from the PSHA model, the improved reliability of seismic design and the reduction in construction and maintenance costs for critical structures are potentially significant. We advocate that PBR validation be used to inform the selection criteria of the appropriate suite of GMMs to include in not only future USGS NSHM updates but future PSHA studies worldwide.

CONCLUSIONS

In order to provide previously elusive earthquake ground-motion constraints on longer-term patterns of seismicity than have been recorded by modern instrumentation, we characterized both the fragility and fragility age of 20 precariously balanced rocks across seismically active southern California. This study presents the largest dataset of rigorously analyzed PBR fragilities and fragility ages yet produced. We conducted a probabilistic fragility assessment of the geometry of each PBR toppling from a range of ground-motion amplitudes (PGA) and periods (PGV/PGA). We then modeled the age at which the 20 precariously balanced rocks developed their current fragile geometries from ~1 to ~50 ka. This distribution of fragility ages not only challenges the previous assumption that most PBRs in southern California are >10 ka, but also reveals that some PBRs have been preserved in the landscape for significantly longer than previously thought. Consequently, this distribution of ages demonstrates the importance of calculating the fragility age of each individual PBR.

We then assessed the probability that each precariously balanced rock, since its formation, survived the estimated ground motions from local seismic sources. The ground-motion estimates for each PBR site were calculated by our PSHA model using the *OpenQuake* seismic hazard and risk engine. Our PSHA model ground motion characterization had 15 GMM end-branches that each estimated different ground-motions levels and each branch was validated individually by the PBR data. The UCERF3 seismic source characterization we used and NGA-West2 GMMs we validated are the inputs to the 2014 and 2018 USGS NSHM, which provides crucial information necessary to disaster preparation, earthquake building codes, insurance rates, and the siting, design, and maintenance of critical facilities in southern California. The UCERF3 seismic source characterization and NGA-West2 GMMs have not as of yet been validated in this way and our study reinforces the value of implementing such validation using PBR data over timescales of thousands to tens of thousands of years.

None of the NGA-West2 GMMs estimated ground motions across southern California that are consistent with all 20 precariously balanced rock data. In other words, each GMM estimated ground-motion levels at a frequency of exceedance that yielded a sufficiently high probability that a subset of the studied still-standing PBRs would have been toppled. We believe our results are compelling evidence of the inherent issues of ground-motion estimates extrapolated beyond any historical recordings and the use of the ergodic assumption in GMMs. Furthermore, the rejection of all 15 GMM ground-motion estimates by seven of our studied PBRs provide evidence that some component of the inconsistent ground-motion estimates is originating from the UCERF3 "true mean" model. Finally, we then investigated the potential improvement to the PSHA ground motion characterization and the resulting ground-motion estimates that could be made by removing the GMM I14 most frequently rejected by our PBR data and, therefore, invalidated. At the annual frequency of exceedance corresponding to a 2% probability of exceedance in 50 years, the 2475 year mean return period pertinent for national seismic safety regulations and building code design standards, we reduced the mean ground-motion estimate by 2-7% and reduced the ground motion uncertainty range for the 5th–95th fractiles by 10-36% at our PBR sites. The opportunity to validate and reject PSHA ground-motion estimates and, in turn, remove the invalid models offers a powerful opportunity to increase the certainty with which such earthquake ground-motion estimates can be made in the future.

ACKNOWLEDGMENTS

This study could not have been carried out without the significant contributions and collaboration of Rasool Anooshehpoor, James Brune, Richard Brune, and Matthew Purvance. In addition, we thank the many researchers who were part of the broader study of southern California precariously balanced rocks, including Sianan Akciz, John Anderson, Ramon Arrowsmith, Glenn Biasi, Jessica Donovan, Victoria Forbes, David Haddad, Tom Hanks, Jon Harvey, Andrew Homan, Thomas Jordan, John McGregor, Corrie Neighbors, Inyo Saleeby, Tyanna Schlom, Mark Stirling, Gillian Thompson and Flowra Zhang. We thank Marco Pagani and Anirudh Rao (GEM Foundation) for assistance with and access to the *OpenQuake* "true mean" UCERF3 model. Funding for this work was provided by Southern California Earthquake Center (SCEC) Award no. 07110 (to Lisa Grant Ludwig), 08094 (to Lisa Grant Ludwig and Lesley Perg), 09113 (to Lisa Grant Ludwig, Dylan H. Rood, James Brune and Katherine Kendrick), 10118 (to Lisa Grant Ludwig and James Brune), 11070 (to Lisa Grant Ludwig and Dylan Rood), 12073 (to Glenn Biasi and Lisa Grant Ludwig), 12088 (Mark Stirling and Dylan Rood), 13062 (Mark Stirling and Dylan Rood), 13069 (to Lisa Grant Ludwig and Thomas Jordan), a Lawrence Livermore National Laboratory Lawrence Scholar Program Fellowship (to Dylan Rood), NSF Postdoctoral Fellowship Award no. EAR-0948350 (to Dylan Rood), by the Ann and Gordon Getty Foundation, and a studentship provided by the EPSRC Doctoral Training Partnership no. EP/N509486/1 (to Anna Rood). Portions of this work were performed under the auspices of the U.S. Department of Energy Lawrence Livermore National Laboratory under Contract DE-AC52-07NA27344. SCEC is funded by NSF Cooperative Agreement EAR-0106924 and U.S. Geological Survey Cooperative Agreement 02HQAG0008. The authors also acknowledge the financial support from the Australian Government for the Centre for Accelerator Science at the Australian Nuclear Science and Technology Organisation (ANSTO) through the National Collaborative Research Infrastructure Strategy (NCRIS). This work was completed thanks to ANSTO Award Number

AP11387 (to Anna H. Rood, Dylan H. Rood, and Klaus M. Wilcken). We thank the staff of the Center for Accelerator Mass Spectrometry (CAMS) at Lawrence Livermore National Laboratory (LLNL) and the Scottish Universities Environmental Research Centre (SUERC) for their support during isotopic analyses. This is SCEC contribution number XXXXX. Any use of trade, firm, or product names is for descriptive purposes only and does not imply endorsement by the U.S. Government.

REFERENCES CITED

Abbott, E., Horspool, N., Gerstenberger, M., Huso, R., Van Houtte, C., McVerry, G., & Canessa, S. (2020). Challenges and opportunities in New Zealand seismic hazard and risk modeling using OpenQuake. *Earthquake Spectra, 36*(1_suppl), 210-225. doi:10.1177/8755293020966338

Abrahamson, N. A., & Bhasin, S. (2020). *Conditional ground-motion model for peak ground velocity for active crustal regions*. Retrieved from https://peer.berkeley.edu/sites/default/files/2020_05_abrahamson_final.pdf

Abrahamson, N. A., Silva, W. J., & Kamai, R. (2014). Summary of the ASK14 Ground Motion Relation for Active Crustal Regions. *Earthquake Spectra, 30*(3), 1025-1055. doi:10.1193/070913eqs198m

Allen, T. I., Halchuk, S., Adams, J., & Weatherill, G. A. (2020). Forensic PSHA: Benchmarking Canada's Fifth Generation seismic hazard model using the OpenQuake-engine. *Earthquake Spectra, 36*(1_suppl), 91-111. doi:10.1177/8755293019900779

Anderson, J. G., & Brune, J. N. (1999). Probabilistic Seismic Hazard Analysis without the Ergodic Assumption. *Seismological Research Letters, 70*(1), 19-28. doi:10.1785/gssrl.70.1.19

Anooshehpoor, A., Brune, J., & Zeng, Y. (2004). Methodology for Obtaining Constraints on Ground Motion from Precariously Balanced Rocks. *Bulletin of the Seismological Society of America, 94*, 285-303. doi:10.1785/0120020242

Anooshehpoor, A., Brune, J. N., Daemen, J., & Purvance, M. D. (2013). Constraints on Ground Accelerations Inferred from Unfractured Hoodoos near the Garlock Fault, California. *Bulletin of the Seismological Society of America, 103*(1), 99-106. doi:10.1785/0120110246

Atkinson, G. M., Bommer, J. J., & Abrahamson, N. A. (2014). Alternative Approaches to Modeling Epistemic Uncertainty in Ground Motions in Probabilistic Seismic-Hazard Analysis. *Seismological Research Letters, 85*(6), 1141-1144. doi:10.1785/0220140120

Baker, J. W., Abrahamson, N. A., Whitney, J. W., Board, M. P., & Hanks, T. C. (2013). Use of Fragile Geologic Structures as Indicators of Unexceeded Ground Motions and Direct Constraints on Probabilistic Seismic Hazard Analysis. *Bulletin of the Seismological Society of America, 103*(3), 1898-1911. doi:10.1785/0120120202

Balco, G. (2014). Simple computer code for estimating cosmic-ray shielding by oddly shaped objects. *Quaternary Geochronology, 22*, 175-182. doi:10.1016/j.quageo.2013.12.002

Balco, G. (2017). Production rate calculations for cosmic-ray-muon-produced 10Be and 26Al benchmarked against geological calibration data. *Quaternary Geochronology, 39*, 150-173. doi:10.1016/j.quageo.2017.02.001

Balco, G., Purvance, M. D., & Rood, D. H. (2011). Exposure dating of precariously balanced rocks. *Quaternary Geochronology, 6*(3), 295-303. doi:10.1016/j.quageo.2011.03.007

Balco, G., Purvance, M. D., & Rood, D. H. (2012). Corrigendum to "Exposure dating of precariously balanced rocks" [Quaternary Geochronology 6 (2011) 295–303]. *Quaternary Geochronology, 9*, 86. doi:10.1016/j.quageo.2012.02.011

Balco, G., Stone, J. O., Lifton, N. A., & Dunai, T. J. (2008). A complete and easily accessible means of calculating surface exposure ages or erosion rates from 10Be and 26Al measurements. *Quaternary Geochronology, 3*(3), 174-195. doi:10.1016/j.quageo.2007.12.001

Bell, J. W., Brune, J. N., Liu, T., Zreda, M., & Yount, J. C. (1998). Dating precariously balanced rocks in seismically active parts of California and Nevada. *Geology, 26*(6), 495-498. doi:10.1130/0091-7613(1998)026<0495:Dpbris>2.3.Co;2

Bierman, P. R., & Steig, E. J. (1996). Estimating Rates of Denundation Using Cosmogenic Isotope Abundances In Sediment. *Earth Surface Processes and Landforms, 21*, 125-139.

Binnie, S. A., Phillips, W. M., Summerfield, M. A., & Fifield, L. K. (2007). Tectonic uplift, threshold hillslopes, and denudation rates in a developing mountain range. *Geology, 35*(8). doi:10.1130/g23641a.1

Blythe, Burbank, Farley, & Fielding. (2000). Structural and topographic evolution of the central Transverse Ranges, California, from apatite fission-track, (U–Th)/He and digital elevation model analyses. *Basin Research, 12*(2), 97-114. doi:https://doi.org/10.1046/j.1365-2117.2000.00116.x

Bommer, J. J., Abrahamson, N. A., Strasser, F. O., Pecker, A., Bard, P.-Y., Bungum, H., et al. (2004). The Challenge of Defining Upper Bounds on Earthquake Ground Motions. *Seismological Research Letters, 75*(1), 82-95. doi:10.1785/gssrl.75.1.82

Bommer, J. J., Douglas, J., Scherbaum, F., Cotton, F., Bungum, H., & Fäh, D. (2010). On the Selection of Ground-Motion Prediction Equations for Seismic Hazard Analysis. *Seismological Research Letters, 81*(5), 783-793. doi:10.1785/gssrl.81.5.783

Boore, D. M., Stewart, J. P., Seyhan, E., & Atkinson, G. M. (2014). NGA-West2 Equations for Predicting PGA, PGV, and 5% Damped PSA for Shallow Crustal Earthquakes. *Earthquake Spectra, 30*(3), 1057-1085. doi:10.1193/070113eqs184m

Borchers, B., Marrero, S., Balco, G., Caffee, M., Goehring, B., Lifton, N., et al. (2016). Geological calibration of spallation production rates in the CRONUS-Earth project. *Quaternary Geochronology, 31*, 188-198. doi:10.1016/j.quageo.2015.01.009

Bozorgnia, Y., Abrahamson, N. A., Atik, L. A., Ancheta, T. D., Atkinson, G. M., Baker, J. W., et al. (2014). NGA-West2 Research Project. *Earthquake Spectra, 30*(3), 973-987. doi:10.1193/072113eqs209m

Brune, J. N. (1996). Precariously balanced rocks and ground-motion maps for Southern California. *Bulletin of the Seismological Society of America, 86*(1A), 43-54. doi:10.1785/BSSA08601A0043

Campbell, K. W., & Bozorgnia, Y. (2008). NGA Ground Motion Model for the Geometric Mean Horizontal Component of PGA, PGV, PGD and 5% DampedLinear Elastic Response Spectra for Periods Ranging from 0.01 to 10 s. *Earthquake Spectra, 24*(1), 139-171. doi:10.1193/1.2857546

Campbell, K. W., & Bozorgnia, Y. (2014). NGA-West2 Ground Motion Model for the Average Horizontal Components of PGA, PGV, and 5% Damped Linear Acceleration Response Spectra. *Earthquake Spectra, 30*(3), 1087-1115. doi:10.1193/062913eqs175m

Chiou, B. S. J., & Youngs, R. R. (2014). Update of the Chiou and Youngs NGA Model for the Average Horizontal Component of Peak Ground Motion and Response Spectra. *Earthquake Spectra, 30*(3), 1117-1153. doi:10.1193/072813eqs219m

Corbett, L., Bierman, P., & Rood, D. (2016). An approach for optimizing in situ cosmogenic 10Be sample preparation. *Quaternary Geochronology, 33*, 24-34. doi:10.1016/j.quageo.2016.02.001

Cornell, C. A. (1968). Engineering seismic risk analysis. *Bulletin of the Seismological Society of America, 58*(5), 1583-1606. doi:10.1785/BSSA0580051583

DeMets, C., Gordon, R. G., & Argus, D. F. (2010). Geologically current plate motions. *Geophysical Journal International, 181*(1), 1-80. doi:10.1111/j.1365-246X.2009.04491.x

DiBiase, R. A., Whipple, K. X., Heimsath, A. M., & Ouimet, W. B. (2010). Landscape form and millennial erosion rates in the San Gabriel Mountains, CA. *Earth and Planetary Science Letters, 289*(1-2), 134-144. doi:10.1016/j.epsl.2009.10.036

Dolan, J. F., Bowman, D. D., & Sammis, C. G. (2007). Long-range and long-term fault interactions in Southern California. *Geology, 35*(9), 855-858. doi:10.1130/g23789a.1

Douglas, J., & Edwards, B. (2016). Recent and future developments in earthquake ground motion estimation. *Earth-Science Reviews, 160*, 203-219. doi:10.1016/j.earscirev.2016.07.005

Dunai, T. J. (2010). *Cosmogenic Nuclides: Principles, Concepts and Applications in the Earth Surface Sciences*: Cambridge University Press.

DuRoss, C. B., Gold, R. D., Dawson, T. E., Scharer, K. M., Kendrick, K. J., Akciz, S. O., et al. (2020). Surface Displacement Distributions for the July 2019 Ridgecrest, California, Earthquake Ruptures. *Bulletin of the Seismological Society of America, 110*(4), 1400-1418. doi:10.1785/0120200058

ESRI (Environmental Systems Research Institute). (2020). ArcGIS Desktop: Version 10.8.

Field, E. H., Biasi, G. P., Bird, P., Dawson, T. E., Felzer, K. R., David D. Jackson, et al. (2013). *Uniform California earthquake rupture forecast, version 3 (UCERF3)—The time-independent model* (U.S. Geological Survey Open-File Report 2013–1165). Retrieved from http://pubs.usgs.gov/of/2013/1165/

Gerstenberger, M. C., Marzocchi, W., Allen, T., Pagani, M., Adams, J., Danciu, L., et al. (2020). Probabilistic Seismic Hazard Analysis at Regional and National Scales: State of the Art and Future Challenges. *Reviews of Geophysics, 58*(2). doi:10.1029/2019rg000653

Grant Ludwig, L., Brune, J. N., Anooshehpoor, A., Purvance, M. D., Brune, R. J., & Lozos, J. C. (2015). Reconciling Precariously Balanced Rocks (PBRs) with Large Earthquakes on the San Andreas Fault System. *Seismological Research Letters, 86*(5), 1345-1353. doi:10.1785/0220140239

Gregor, N., Abrahamson, N. A., Atkinson, G. M., Boore, D. M., Bozorgnia, Y., Campbell, K. W., et al. (2014). Comparison of NGA-West2 GMPEs. *Earthquake Spectra, 30*(3), 1179-1197. doi:10.1193/070113eqs186m

Hall, C. M., Webb, H. N., Girty, G. H., Allam, A. A., & Rockwell, T. K. (2019). A case study of a precariously balanced rock, its partially exhumed corestone platform, and encasing saprock and soil. *Catena, 172*, 719-737. doi:10.1016/j.catena.2018.09.029

Hanks, T. C., Abrahamson, N. A., Baker, J. W., Boore, D. M., Board, M., Brune, J. N., et al. (2013). Extreme ground motions and Yucca Mountain. doi:10.3133/ofr20131245

Hauksson, E., Jones, L. M., & Hutton, K. (1995). The 1994 Northridge earthquake sequence in California: Seismological and tectonic aspects. *Journal of Geophysical Research: Solid Earth, 100*(B7), 12335-12355. doi:https://doi.org/10.1029/95JB00865

Idriss, I. M. (2014). An NGA-West2 Empirical Model for Estimating the Horizontal Spectral Values Generated by Shallow Crustal Earthquakes. *Earthquake Spectra, 30*(3), 1155-1177. doi:10.1193/070613eqs195m

Jacoby, G. C., Sheppard, P. R., & Sieh, K. E. (1988). Irregular recurrence of large earthquakes along the san andreas fault: evidence from trees. *Science, 241*, 196-199. doi:10.1126/science.241.4862.196

Jones, L. M., Bernknopf, R., Cox, D., Goltz, J., Hudnut, K., Mileti, D., et al. (2008). *The ShakeOut Scenario: U.S. Geological Survey Open-File Report 2008-1150 and California Geological Survey Preliminary Report 25*. Retrieved from http://pubs.usgs.gov/of/2008/1150/

Kendrick, K. J., Partin, C. A., & Graham, R. C. (2016). Granitic Boulder Erosion Caused by Chaparral Wildfire: Implications for Cosmogenic Radionuclide Dating of Bedrock Surfaces. *The Journal of Geology, 124*(4), 529-539. doi:10.1086/686273

Kohl, C. P., & Nishiizumi, K. (1992). Chemical isolation of quartz for measurement of in-situ - produced cosmogenic nuclides. *Geochimica et Cosmochimica Acta, 56*(9), 3583-3587. doi:10.1016/0016-7037(92)90401-4

Lal, D. (1991). Cosmic ray labeling of erosion surfaces: in situ nuclide production rates and erosion models. *Earth and Planetary Science Letters, 104*(2), 424-439. doi:10.1016/0012-821X(91)90220-C

Marshall, J. A., Roering, J. J., Gavin, D. G., & Granger, D. E. (2017). Late Quaternary climatic controls on erosion rates and geomorphic processes in western Oregon, USA. *GSA Bulletin, 129*(5-6), 715-731. doi:10.1130/B31509.1

Nishiizumi, K., Imamura, M., Caffee, M. W., Southon, J. R., Finkel, R. C., & McAninch, J. (2007). Absolute calibration of 10Be AMS standards. *Nuclear Instruments and Methods in Physics Research Section B: Beam Interactions with Materials and Atoms, 258*(2), 403-413. doi:10.1016/j.nimb.2007.01.297

Oberlander, T. M. (1972). Morphogenesis of Granitic Boulder Slopes in the Mojave Desert, California. *The Journal of Geology, 80*(1), 1-20.

Pagani, M., Monelli, D., Weatherill, G., Danciu, L., Crowley, H., Silva, V., et al. (2014). OpenQuake Engine: An Open Hazard (and Risk) Software for the Global Earthquake Model. *Seismological Research Letters, 85*(3), 692-702. doi:10.1785/0220130087

Petersen, M. D., Moschetti, M. P., Powers, P. M., Mueller, C. S., Haller, K. M., Frankel, A. D., et al. (2014). *Documentation for the 2014 Update of the United States National Seismic Hazard Maps* (U.S. Geological Survey Open-File Report 2014–1091). Retrieved from http://dx.doi.org/10.333/ofr20141091

Petersen, M. D., Shumway, A. M., Powers, P. M., Mueller, C. S., Moschetti, M. P., Frankel, A. D., et al. (2020). The 2018 update of the US National Seismic Hazard Model: Overview of model and implications. *Earthquake Spectra, 36*(1), 5-41. doi:10.1177/8755293019878199

PhotoModeler Technologies. (2018). PhotoModeler Scanner (Version 2018.1.2). Retrieved from https://www.photomodeler.com/

Powell, R. E., & Weldon, R. J. (1992). EVOLUTION OF THE SAN ANDREAS FAULT. *Annual Review of Earth and Planetary Sciences, 20*(1), 431-468. doi:10.1146/annurev.ea.20.050192.002243

Purvance, M. D., Anooshehpoor, A., & Brune, J. N. (2008a). Freestanding block overturning fragilities: Numerical simulation and experimental validation. *Earthquake Engineering and Structural Dynamics, 37*(5), 791-808. doi:10.1002/eqe.789

Purvance, M. D., Brune, J. N., Abrahamson, N. A., & Anderson, J. G. (2008b). Consistency of Precariously Balanced Rocks with Probabilistic Seismic Hazard Estimates in Southern California. *Bulletin of the Seismological Society of America, 98*(6), 2629-2640. doi:10.1785/0120080169

Rao, A. S., Weatherill, G., Silva, V., & Schneider, J. (2017). *Beyond Button Pushing Seismic Risk Assessment for California* (GEM Technical Report 2017 V1.0.0). Retrieved from

Rood, A. H., Rood, D. H., Stirling, M. W., Madugo, C. M., Abrahamson, N. A., Wilcken, K. M., et al. (2020). Earthquake Hazard Uncertainties Improved Using Precariously Balanced Rocks. *AGU Advances, 1*(4). doi:10.1029/2020av000182

Rood, D. H., Hall, S., Guilderson, T. P., Finkel, R. C., & Brown, T. A. (2010). Challenges and opportunities in high-precision Be-10 measurements at CAMS. *Nuclear Instruments and Methods in Physics Research Section B: Beam Interactions with Materials and Atoms, 268*(7), 730-732. doi:10.1016/j.nimb.2009.10.016

Sieh, K., Stuiver, M., & Brillinger, D. (1989). A more precise chronology of earthquakes produced by the San Andreas Fault in southern California. *Journal of Geophysical Research, 94*(B1). doi:10.1029/JB094iB01p00603

SSHAC, S. S. H. A. C. (2012). *Practical Implementation Guidelines for SSHAC Level 3 and 4 Hazard Studies*. Retrieved from https://www.nrc.gov/docs/ML1211/ML12118A445.pdf

Stafford, P. J. (2018). Continuous integration of data into ground-motion models using Bayesian updating. *Journal of Seismology, 23*(1), 39-57. doi:10.1007/s10950-018-9792-3

Stirling, M. W., Abbott, E. R., Rood, D. H., McVerry, G. H., Abrahamson, N. A., Barrell, D. J. A., et al. (2021). First Use of Fragile Geologic Features to Set the Design Motions for a Major Existing Engineered Structure. *Bulletin of the Seismological Society of America*. doi:10.1785/0120210026

Stirling, M. W., Anooshehpoor, A., Brune, J. N., Biasi, G. P., & Wesnousky, S. G. (2002). Assessment of the Site Conditions of Precariously Balanced Rocks in the Mojave Desert, Southern California. *Bulletin of the Seismological Society of America, 92*(6), 2139–2214. doi:10.1785/0120010221

Stone, J. O. (2000). Air pressure and cosmogenic isotope production. *Journal of Geophysical Research: Solid Earth, 105*(B10), 23753-23759. doi:10.1029/2000JB900181

The Mathworks Inc. (2016). MATLAB (Version Version 2016b). Retrieved from https://uk.mathworks.com/downloads/

Thompson, E. M., Wald, D. J., & Worden, C. B. (2014). A VS30 Map for California with Geologic and Topographic Constraints. *Bulletin of the Seismological Society of America, 104*(5), 2313-2321. doi:10.1785/0120130312

Veeraraghavan, S., Hudnut, K. W., & Krishnan, S. (2017). Toppling Analysis of the Echo Cliffs Precariously Balanced Rock. *Bulletin of the Seismological Society of America, 107*(1), 72-84. doi:10.1785/0120160169

Wilcken, K. M., Fink, D., Hotchkis, M. A. C., Garton, D., Button, D., Mann, M., et al. (2017). Accelerator Mass Spectrometry on SIRIUS: New 6MV spectrometer at ANSTO. *Nuclear Instruments and Methods in Physics Research Section B: Beam Interactions with Materials and Atoms, 406*, 278-282. doi:10.1016/j.nimb.2017.01.003

Xu, S., Freeman, S. P. H. T., Rood, D. H., & Shanks, R. P. (2015). Decadal 10Be, 26Al and 36Cl QA measurements on the SUERC 5MV accelerator mass spectrometer. *Nuclear Instruments and Methods in Physics Research Section B: Beam Interactions with Materials and Atoms, 361*, 39-42. doi:10.1016/j.nimb.2015.03.064

Zielke, O., Arrowsmith, J. R., Grant Ludwig, L., & Akciz, S. O. (2012). High-Resolution Topography-Derived Offsets along the 1857 Fort Tejon Earthquake Rupture Trace, San Andreas Fault. *Bulletin of the Seismological Society of America, 102*(3), 1135-1154. doi:10.1785/0120110230

FIGURE CAPTIONS

Figure 1. Regional map of southern California with fault traces of the UCERF3 seismic source characterization (Field et al., 2013) that contribute to the region's seismic hazard shown in red. Major faults and fault zones are named in red. Mountain ranges are named in black and major cities in black bold. The San Gabriel and San Bernardino Mountains are a part of the Transverse Ranges. Blue symbols show the location of the studied PBRs, each labelled with the rock's ID (Table 1). Each of the five regions have different dominant seismic sources that are being tested by the PBR data. The dominant seismic source in Region 1 (triangles) is the San Andreas fault. Region 2 (squares) is at the junction between the San Andreas, San Jacinto, and Transverse Ranges thrust faults. The dominant seismic source in Region 3 (diamonds) is the Pinto Mountain fault. Region 4 (stars) is between the San Andreas and San Jacinto faults. Region 5 (circles) is between the San Jacinto and Elsinore faults. Inset map of California shows location of Figure 1.

Figure 2. (A) Field photo of the most slender view of representative precariously balanced rock (PBR) GV2 on its pedestal compared to the 3-D model constructed of the rock using photogrammetry. (B) Area of the PBR 3-D model showing the surface that is in contact with the pedestal, i.e., viewing from below the base of the rock up towards the center of mass, labelled with measured geometric parameters required for toppling calculations. Gray circles are the critical rocking points that define the narrowest basal 2-D section through the center of mass (yellow circle). Alpha values (in radians) are gray text and radius length (in meters) are in yellow. The lowest alpha value is the direction the rock will topple. (C) Fragility function of GV2. The 25^{th}, 50^{th} (median), and 75^{th} percentile ground motions are labeled. Equivalent figures for each of the other studied PBRs are provided in the Supplementary Materials: Figure 1.

Figure 3. (A) Sample locations labelled as blue circles on a field photo of each PBR. See Supplementary Materials: Figure 1 for details about which samples are located on the PBR and the pedestal. (B) Graphs show ^{10}Be concentration (x-axis) and depth below PBR top (y-axis). Left graph shows the components of the total predicted nuclide concentration attributable to different phases of PBR exhumation. Blue line is before

exhumation, yellow line is during exhumation, and gray line is after exhumation. Right graph shows the measured nuclide concentrations in sample (blue circles) compared with those predicted by the forward model best-fitting parameters (open black circles). Light gray circles are samples that were not used in the modeling of PBR exhumation – see Supplementary Materials : Figure 1 for details. Yellow circles are the measured concentration in the saprolite sample plotted at the approximate height in the landscape relative to the PBR. Error bars show 1σ uncertainty on measured nuclide concentrations; error bars that are not visible are equal to or smaller than the size of the symbols. The horizontal dashed line is the height of the lowest point on the PBR-pedestal contact. See Supplementary Materials: Figure 1 for discussion about the quality of fit between the measured and modeled ^{10}Be concentrations for each PBR. (C) Histogram of t_{tip} age, in ka, calculated by each of the 400 Monte Carlo iterations. Cumulative black curve of output t_{tip} ages are labelled at the 16th, median (50th), and 84th percentile ages.

Figure 4. The median fragility age, t_{tip} in ka, calculated of each studied PBR is shown as a black diamond. Uncertainty bars are the Monte Carlo modeled 68% confidence intervals, i.e., 16th percentile and 84th percentile fragility ages. Histogram with blue 10 ka bins on the top of the graph show the general distribution of fragility ages.

Figure 5. Histogram of $\varepsilon_{0,sp}$ erosion rate results in blue and ε_1 erosion rate results in gray for each PBR. Apparent erosion rates calculated from sediment samples are shown in yellow. The yellow box extends 1 sigma either side of the vertical mean line and horizontal lines extend 2 sigma. Apparent stream sediment erosion rates are calculated by Version 3 of the online exposure age calculator described by Balco et al. (2008) and subsequently updated.

Figure 6. (A) Hazard curves computed by the OpenQuake engine (Pagani et al., 2014) for the location of GV2. The lower (dotted line), central (solid line), and upper (dashed line) are plotted for each GMM as well as the weighted mean hazard curve (yellow line). Each hazard curve is produced by the "true mean" UCERF3 source characterization with each GMM branch of the ground motion characterization logic tree (Field et al., 2013; Rao et al., 2017). The spread between the upper and lower backbone hazard curves for each GMM represents the epistemic uncertainty in the ground motions estimated by that GMM. (B) The hazard curves for the location of GV2 (the same curves as in A) colored by whether they pass the PBR validation, i.e., the ground-motion estimates are consistent with a 5% probability of survival of GV2, or fail the PBR validation, i.e., the ground-motion estimates are inconsistent with a 5% probability of survival of GV2. Equivalent figures of the other studied PBRs are provided in the Supplementary Materials: Figure 1.

Figure 1

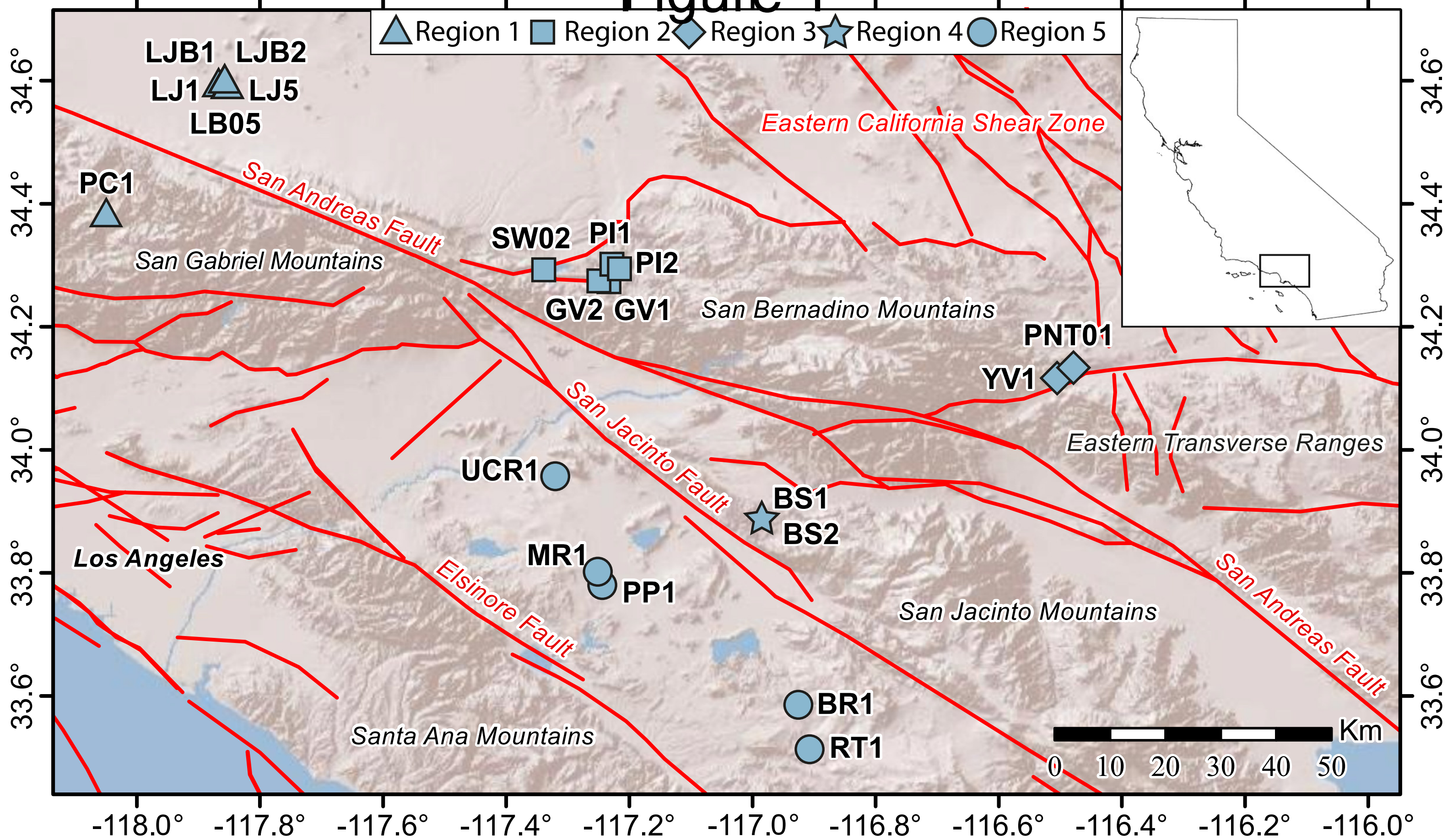
Region 1
Region 2
Region 3
Region 4
Region 5
LJB1
LJB2
LJ1
LJ5
LB05
PC1
SW02
PI1
PI2
GV2
GV1
PNT01
YV1
UCR1
BS1
BS2
MR1
PP1
BR1
RT1
San Andreas Fault
San Gabriel Mountains
Eastern California Shear Zone
San Bernadino Mountains
Eastern Transverse Ranges
San Jacinto Fault
Los Angeles
Elsinore Fault
San Jacinto Mountains
San Andreas Fault
Santa Ana Mountains
Km
0 10 20 30 40 50
-118.0° -117.8° -117.6° -117.4° -117.2° -117.0° -116.8° -116.6° -116.4° -116.2° -116.0°
34.6° 34.4° 34.2° 34.0° 33.8° 33.6°

Figure 2

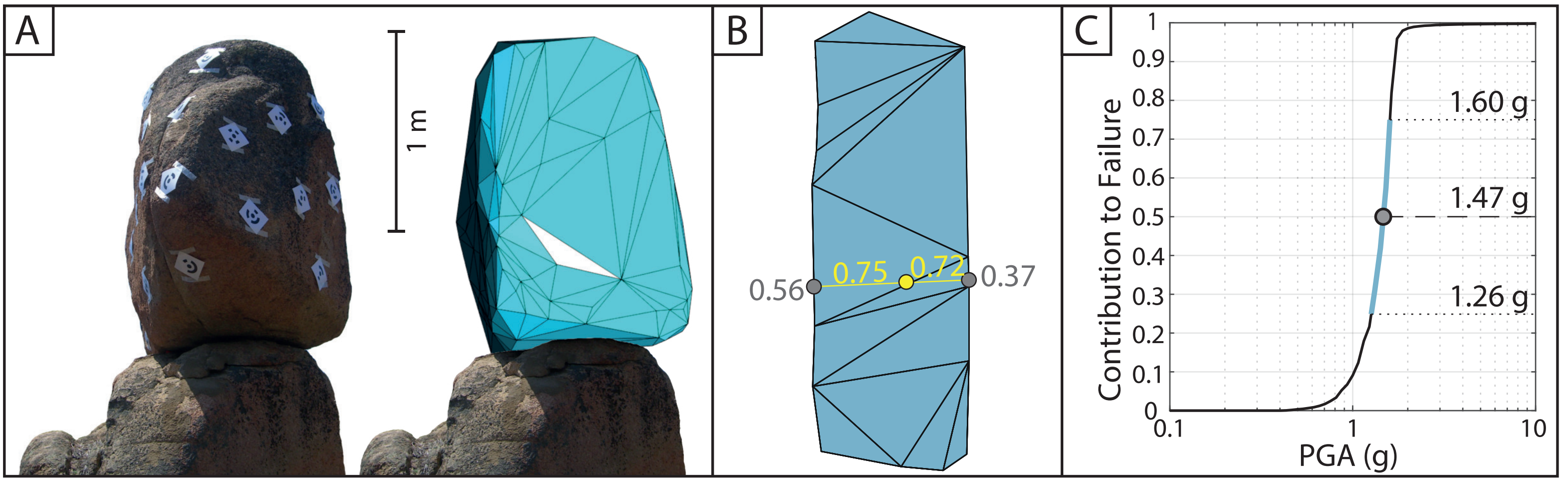

A
1 m
B
0.56
0.75
0.72
0.37
C
Contribution to Failure
PGA (g)
1.60 g
1.47 g
1.26 g
0.1
1
10

Figure 3

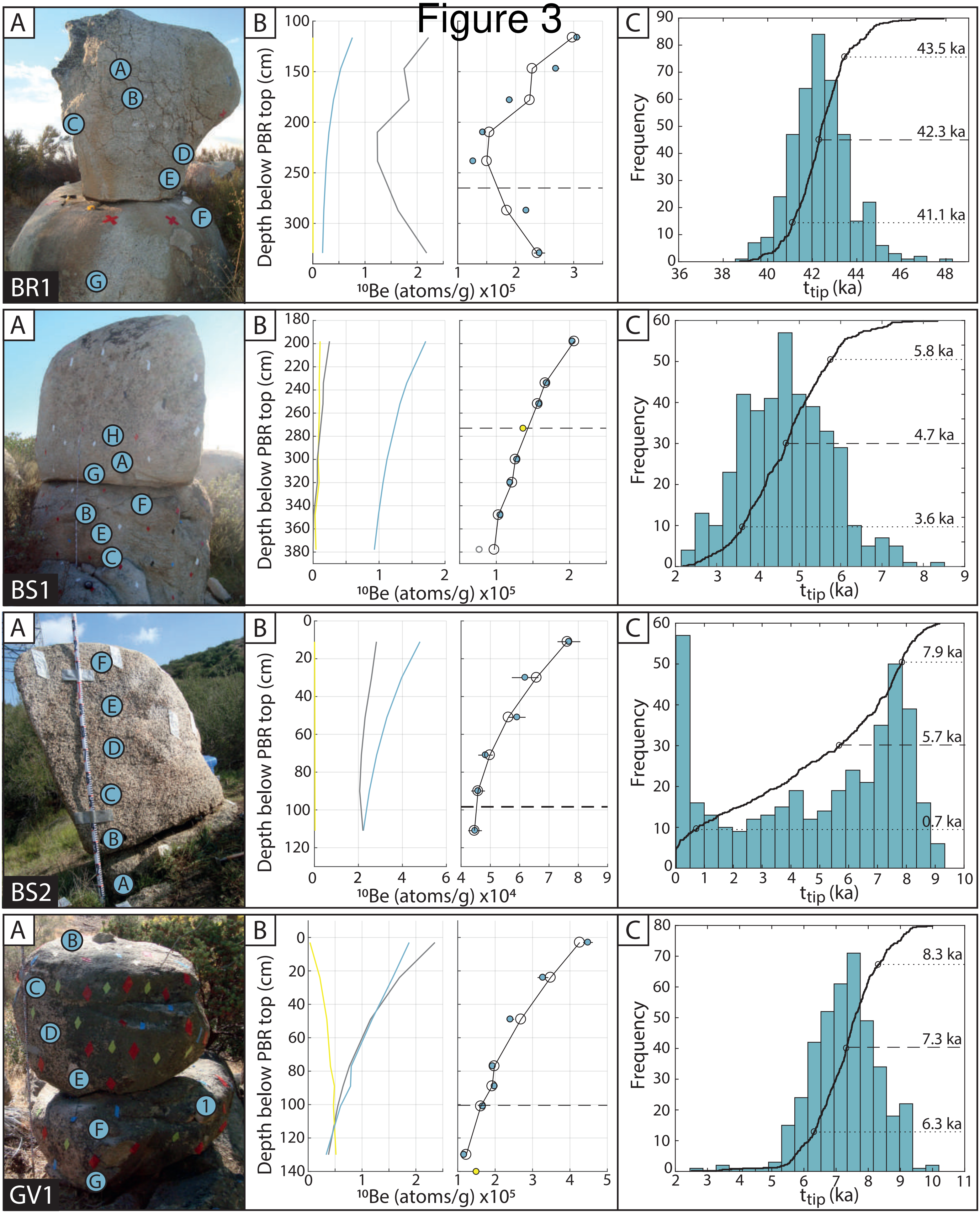

A
B
C
BR1
BS1
BS2
GV1
Depth below PBR top (cm)
¹⁰Be (atoms/g) x10⁵
¹⁰Be (atoms/g) x10⁴
Frequency
t_tip (ka)
43.5 ka
42.3 ka
41.1 ka
5.8 ka
4.7 ka
3.6 ka
7.9 ka
5.7 ka
0.7 ka
8.3 ka
7.3 ka
6.3 ka

Figure 3

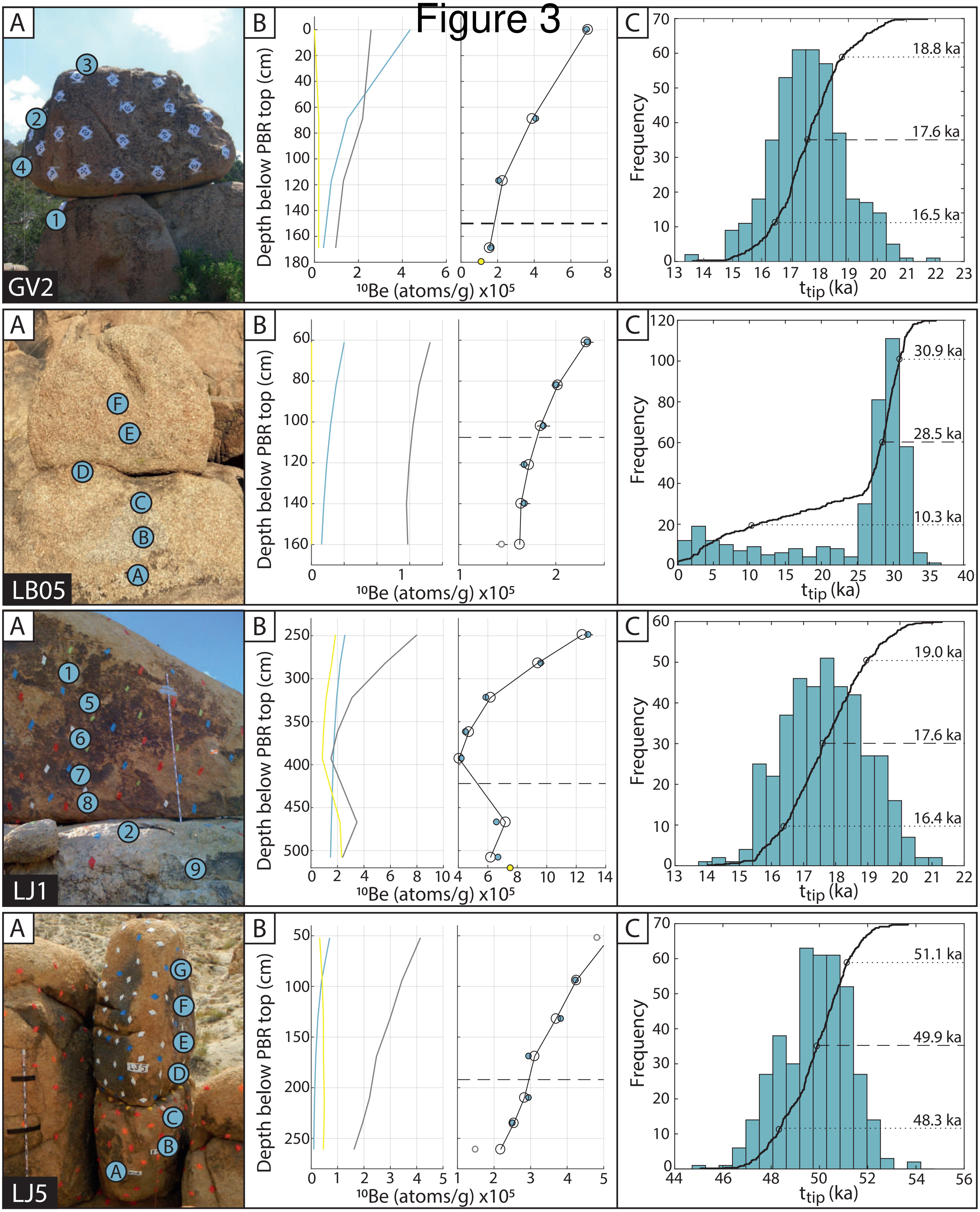

A
B
C
GV2
LB05
LJ1
LJ5
Depth below PBR top (cm)
¹⁰Be (atoms/g) x10⁵
Frequency
t_tip (ka)
18.8 ka
17.6 ka
16.5 ka
30.9 ka
28.5 ka
10.3 ka
19.0 ka
17.6 ka
16.4 ka
51.1 ka
49.9 ka
48.3 ka

Figure 3

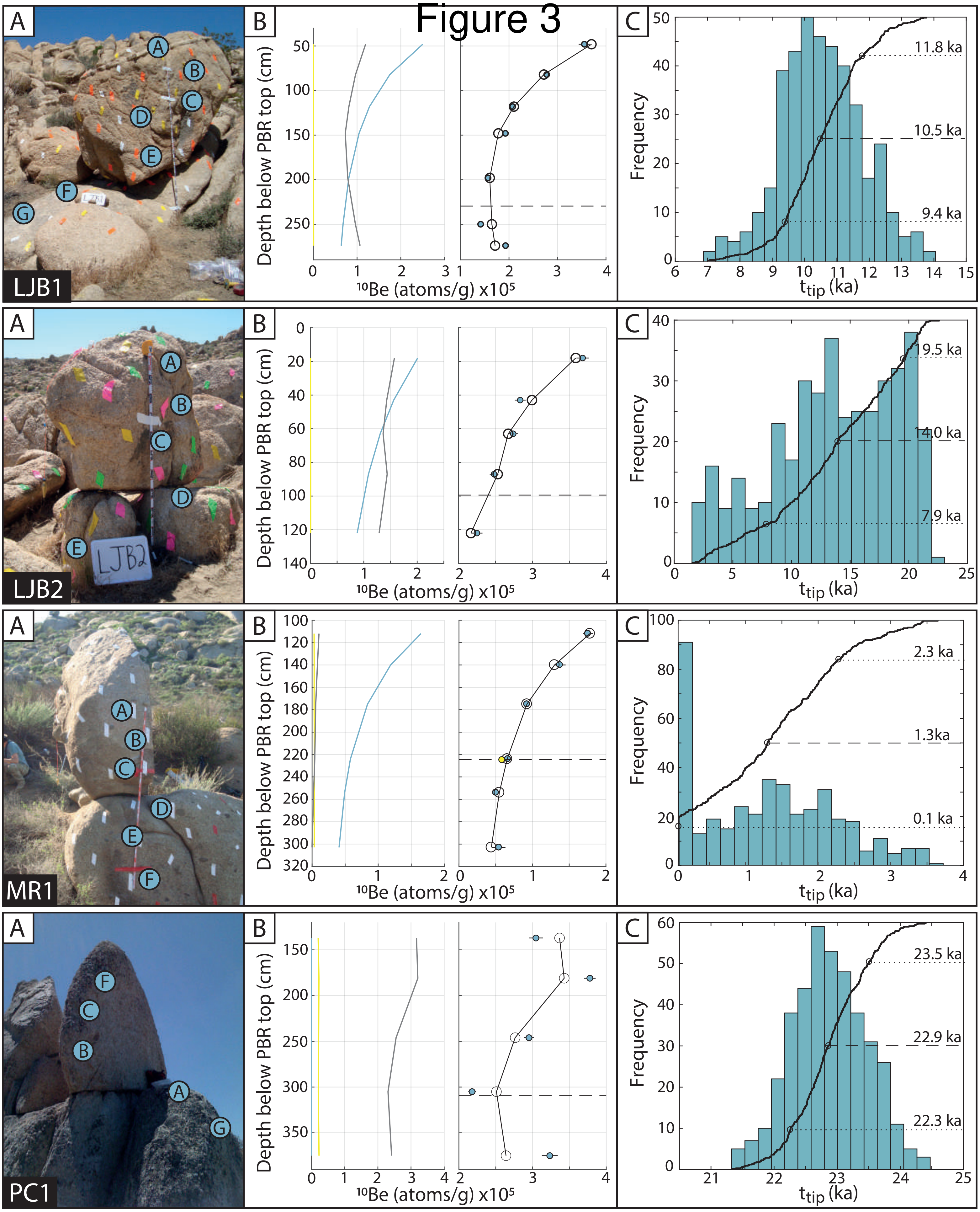

LJB1
LJB2
MR1
PC1
A
B
C
D
E
F
G
Depth below PBR top (cm)
¹⁰Be (atoms/g) x10⁵
Frequency
t_tip (ka)
11.8 ka
10.5 ka
9.4 ka
19.5 ka
14.0 ka
7.9 ka
2.3 ka
1.3ka
0.1 ka
23.5 ka
22.9 ka
22.3 ka

Figure 3

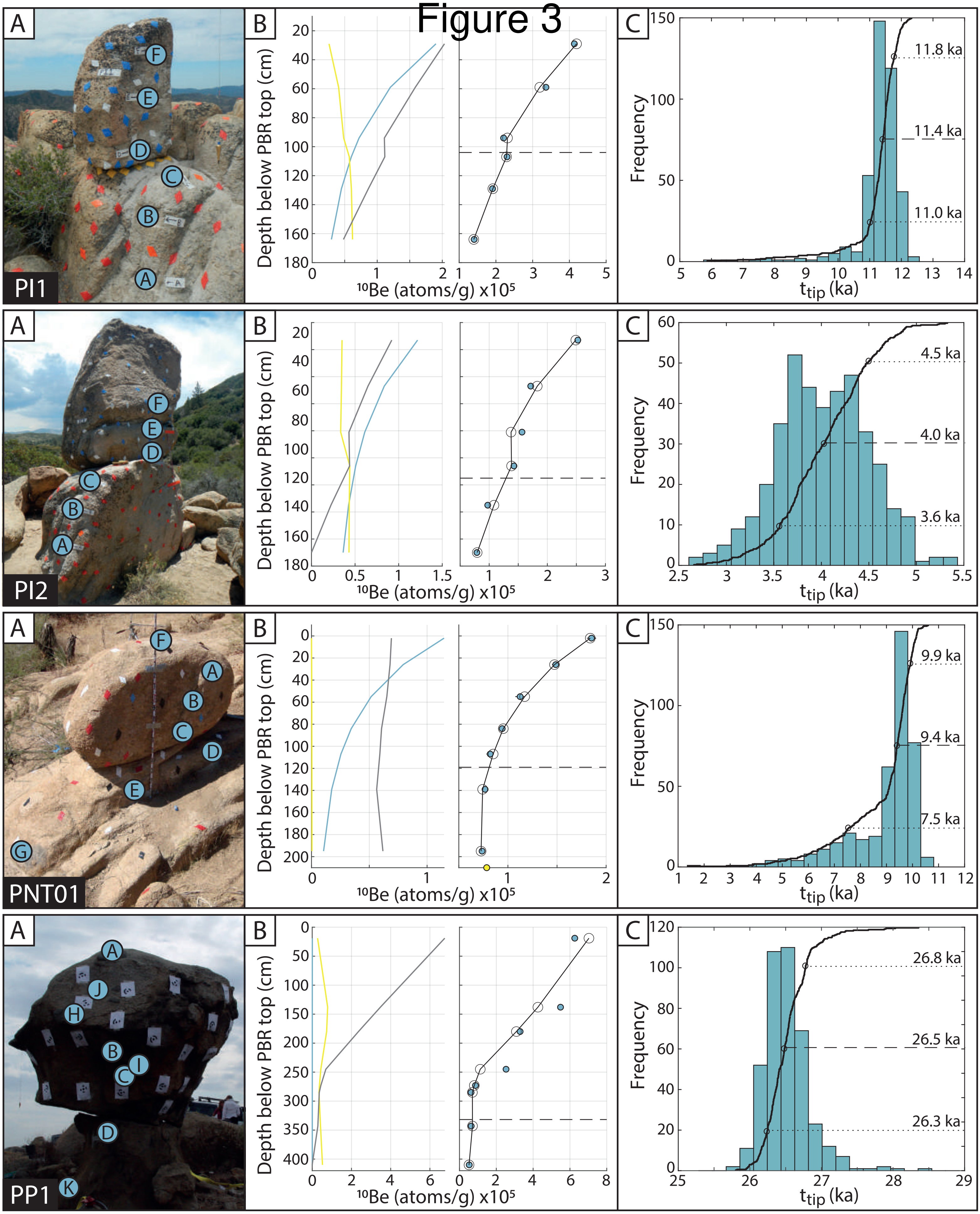
PI1
PI2
PNT01
PP1
Depth below PBR top (cm)
¹⁰Be (atoms/g) x10⁵
Frequency
t_tip (ka)
11.8 ka
11.4 ka
11.0 ka
4.5 ka
4.0 ka
3.6 ka
9.9 ka
9.4 ka
7.5 ka
26.8 ka
26.5 ka
26.3 ka

Figure 3

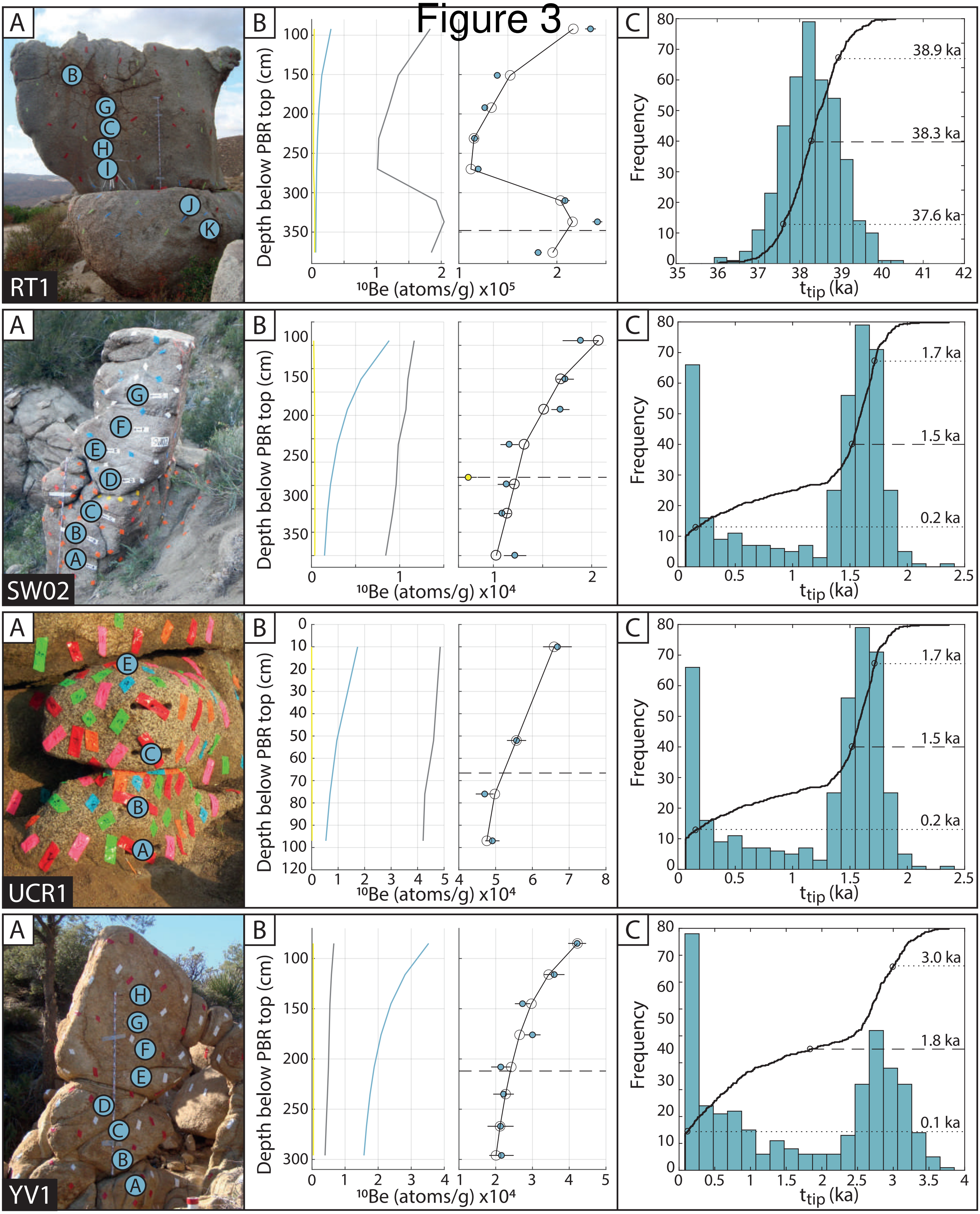

RT1
SW02
UCR1
YV1
Depth below PBR top (cm)
10Be (atoms/g) x10^5
10Be (atoms/g) x10^4
Frequency
t_tip (ka)
38.9 ka
38.3 ka
37.6 ka
1.7 ka
1.5 ka
0.2 ka
3.0 ka
1.8 ka
0.1 ka

Figure 4

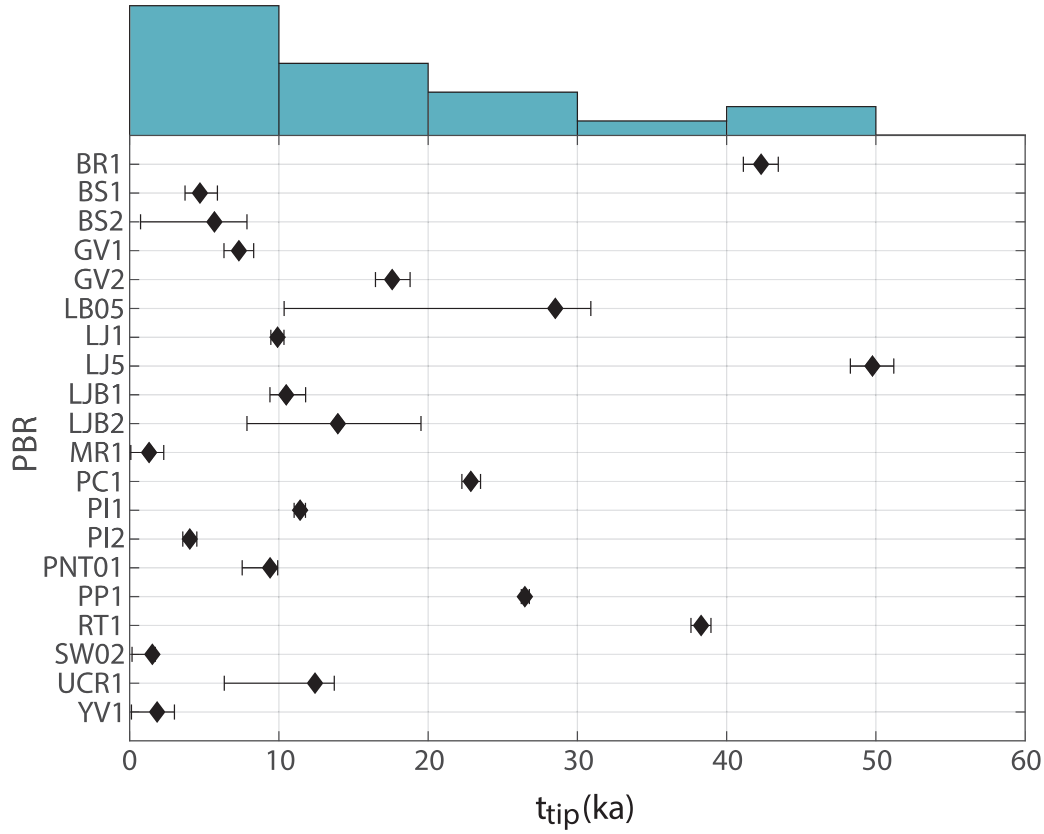

BR1
BS1
BS2
GV1
GV2
LB05
LJ1
LJ5
LJB1
LJB2
MR1
PC1
PI1
PI2
PNT01
PP1
RT1
SW02
UCR1
YV1
PBR
0
10
20
30
40
50
60
t_{tip}(ka)

Figure 5

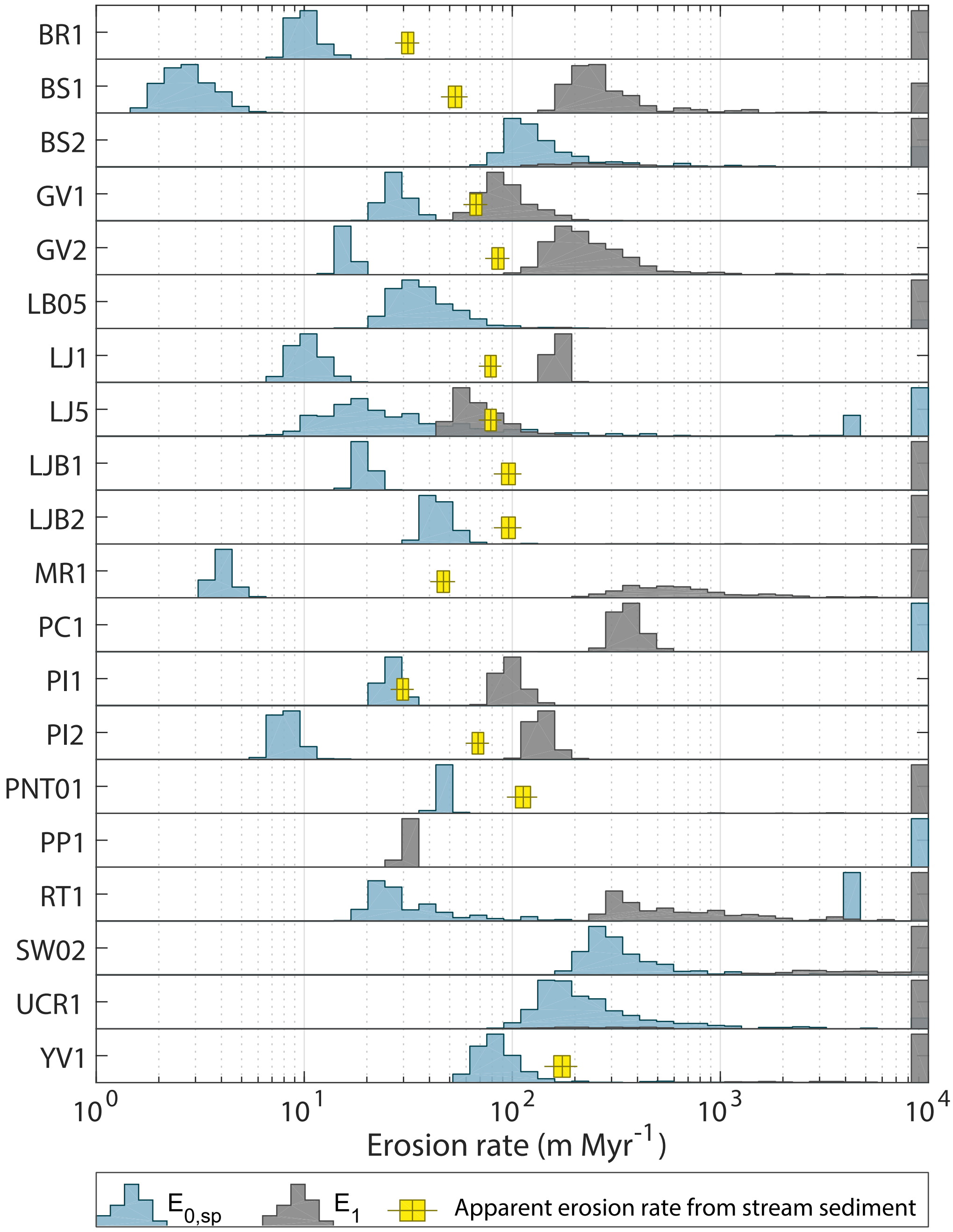
BR1
BS1
BS2
GV1
GV2
LB05
LJ1
LJ5
LJB1
LJB2
MR1
PC1
PI1
PI2
PNT01
PP1
RT1
SW02
UCR1
YV1
10^0
10^1
10^2
10^3
10^4
Erosion rate (m Myr^{-1})
$E_{0,sp}$
E_1
Apparent erosion rate from stream sediment

Figure 6

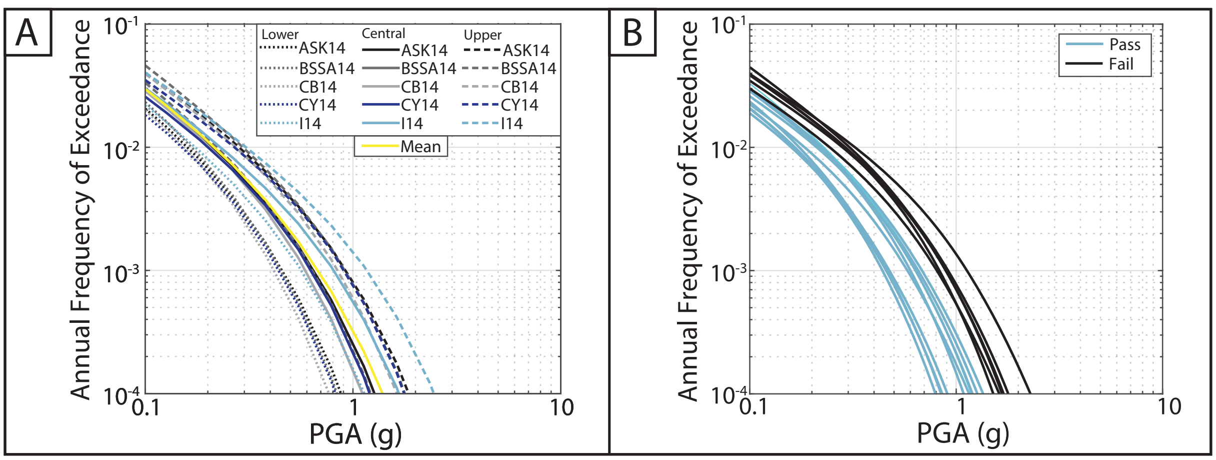

A
Annual Frequency of Exceedance
PGA (g)
Lower
ASK14
BSSA14
CB14
CY14
I14
Central
ASK14
BSSA14
CB14
CY14
I14
Upper
ASK14
BSSA14
CB14
CY14
I14
Mean
B
Pass
Fail

TABLE 1. LOCATION INFORMATION OF THE STUDIED PBRS

Site	PBR ID	Latitude	Longitude	Elevation (m)
Benton Road	BR1	33.59285	-116.92530	778
Beaumont South	BS1	33.89750	-116.98592	759
	BS2	33.89654	-116.98470	734
Grass Valley	GV1	34.27813	-117.23254	1437
	GV2	34.27878	-117.24710	1510
Lovejoy Buttes	LB05	34.59730	-117.86720	882
	LJ1	34.59448	-117.85328	944
	LJ5	34.59454	-117.85199	931
	LJB1	34.60352	-117.85754	1550
	LJB2	34.60316	-117.85705	1534
Motte Rimrock	MR1	33.80942	-117.25282	534
Pacifico Crest	PC1	34.38603	-118.04983	2052
The Pinnacles	PI1	34.30546	-117.22670	1679
	PI2	34.29855	-117.21806	1463
Pioneertown	PNT01	34.13845	-116.47844	1125
Perris	PP1	33.78798	-117.24377	497
Roundtop	RT1	33.52070	-116.90687	734
Silverwood Lake	SW02	34.29688	-117.33979	1107
UC Riverside	UCR1	33.96516	-117.32010	403
Yucca Valley	YV1	34.11756	-116.50897	1280

TABLE 2. MEASURED AND CALCULATED PBR GEOMETRIC PARAMETERS AND FRAGILITY FUNCTION PARAMETERS

PBR	PBR height[†] (m)	Toppling azimuth	α_1 (rad)	α_2 (rad)	R_1 (m)	R_2 (m)	p^2 (s^{-2})	Mean distance[#] (km)	Mean magnitude[#] (Mw)	Median fragility (g)
BR1	2.65	091	0.20	0.27	1.34	1.36	5.47	11.06	6.83	0.64
BS1	2.73	060	0.50	0.58§	1.40	1.35	5.26	8.37	7.35	3.69
BS2[*]	0.98	070	0.25	0.36	0.46	0.46	16.02	8.38	7.35	0.56
GV1	1.00	245	0.43	0.67§	0.49	0.52	14.85	9.95	7.28	1.52
GV2	1.50	192	0.37	0.56§	0.72	0.75	10.27	9.75	7.32	1.47
LB05	1.08	213	0.34	0.47	0.49	0.42	15.10	14.15	7.67	1.01
LJ1	4.22	110	0.31	0.48	1.90	1.55	3.87	14.35	7.65	1.65
LJ5	1.92	344	0.42	0.44	0.87	0.81	8.48	14.40	7.65	1.69
LJB1	2.30	258	0.21	0.42	0.95	0.92	7.71	14.88	7.64	0.66
LJB2	0.99	222	0.16	0.60§	0.46	0.42	15.93	14.87	7.64	0.69
MR1	2.25	334	0.16	0.27	1.06	1.10	6.96	14.98	6.97	0.40
PC1	3.09	264	0.39	0.49	1.15	1.25	6.38	13.91	7.64	1.06
PI1	1.04	241	0.33	0.51§	0.43	0.54	17.03	11.20	7.18	1.06
PI2	2.35	005	0.39	0.44	1.10	1.07	6.69	10.96	7.16	2.01
PNT01	1.19	077	0.26	0.51§	0.49	0.48	15.14	6.46	6.88	0.86
PP1	3.32	222	0.16	0.59§	1.59	1.69	4.62	15.51	6.98	1.01
RT1	3.48	269	0.20	0.37	1.81	1.65	4.07	13.09	6.77	0.93
SW02	1.73	085	0.37	0.62§	0.67	0.89	11.00	7.73	7.45	1.31
UCR1	0.57	265	0.33	0.47	0.29	0.26	25.71	10.76	7.18	0.85
YV1	2.12	239	0.20	0.32	0.96	0.87	7.68	7.08	6.92	0.53

[*]Low confidence PBR fragility geometric parameters, see Discussion section and Supplementary Materials: Figure 1.

[†]PBR height is the measured vertical height from the highest point on the top of the PBR to the lowest point on the PBR-pedestal contact.

§α_2 values of greater than 0.5 radians were set to 0.5 radians in the equations of Purvance et al., (2008a).

[#]Mean distance and magnitude are calculated for a mean return period of 2475 years and V_{S30} conditions of 760 ms^{-1} using the USGS online Unified Hazard Tool.

TABLE 3. SAMPLE-SPECIFIC CONSTANTS AND ^{10}Be CONCENTRATIONS FOR THE GV2 PBR SAMPLES

Sample ID	Sample thickness (cm)*	Distance below PBR top (cm)†	S0,i§	Li (g cm^{-2})§	[Be-10] (atoms/g)	1σ (atoms/g)
GV2-1	5.0	169	0.50	223	163298	3821
GV2-2	4.0	69	0.90	171	410286	6726
GV2-3	4.5	0	0.96	160	688326	15971
GV2-4	3.5	117	0.60	225	207599	4336

*Measured in the field when each sample was collected.
†Vertical height measured from the highest point on the top of the PBR to the sample point.
§Calculated using the code of Balco (2014).

TABLE 4. BEST FIT AND MONTE CARLO MODELED PARAMETER VALUES FOR PBR GV2

Parameter	Best fit	Median	16th	84th
t_0 (ka)	24.7	24.8	23.1	26.4
t_{tip} (ka)	17.7	17.6	16.5	18.8
$\varepsilon_{0,sp}$ (m/Myr)	15.9	15.9	14.8	17.1
$\varepsilon_{0,mu}$ (m/Myr)	39.7	39.5	37.0	42.8
ε_1 (m/Myr)	214.7	206.8	158.8	330.4

Note: Parameters modeled using our updated version of Balco et al. (2011).

TABLE 5. PROBABILITY OF SURVIVAL OF EACH PBR FOR THE GROUND MOTIONS ESTIMATED BY PSHA OUTPUT GROUND-MOTION ESTIMATES (WHITE = PASS, GRAY = FAIL).

		Region 1						Region 2					Region 3		Region 4		Region 5				
	PBR	LB05	LJ1	LJ5	LJB1	LJB2	PC1	GV1	GV2	PI1	PI2	SW02	PNT01	YV1	BS1	BS2	BR1	MR1	PP1	UCR1	RT1
Lower	ASK14	0.06	0.88	0.77	0.11	0.10	0.29	0.88	0.64	0.49	0.96	0.93	0.14	0.20	1.00	0.03	0.00	0.14	0.10	0.27	0.01
	BSSA14	0.12	0.90	0.84	0.14	0.13	0.22	0.93	0.74	0.62	0.98	0.95	0.19	0.18	1.00	0.04	0.00	0.10	0.08	0.31	0.02
	CB14	0.20	0.92	0.87	0.21	0.20	0.68	0.94	0.79	0.66	0.98	0.95	0.15	0.23	1.00	0.08	0.00	0.28	0.27	0.55	0.05
	CY14	0.10	0.91	0.85	0.17	0.15	0.32	0.90	0.70	0.63	0.98	0.94	0.26	0.26	1.00	0.05	0.00	0.19	0.15	0.36	0.04
	I14	0.00	0.78	0.58	0.02	0.02	0.00	0.69	0.29	0.30	0.93	0.80	0.05	0.12	1.00	0.00	0.00	0.03	0.01	0.05	0.00
Central	ASK14	0.00	0.62	0.29	0.00	0.00	0.01	0.60	0.17	0.09	0.87	0.74	0.01	0.03	1.00	0.00	0.00	0.02	0.00	0.01	0.00
	BSSA14	0.00	0.67	0.39	0.00	0.00	0.00	0.69	0.26	0.14	0.90	0.78	0.01	0.02	1.00	0.00	0.00	0.01	0.00	0.01	0.00
	CB14	0.00	0.72	0.51	0.01	0.01	0.13	0.77	0.37	0.23	0.92	0.81	0.01	0.04	1.00	0.00	0.00	0.05	0.03	0.08	0.00
	CY14	0.00	0.68	0.42	0.00	0.00	0.01	0.65	0.23	0.16	0.90	0.76	0.02	0.05	1.00	0.00	0.00	0.02	0.01	0.02	0.00
	I14	0.00	0.42	0.08	0.00	0.00	0.00	0.30	0.02	0.02	0.78	0.48	0.00	0.01	1.00	0.00	0.00	0.00	0.00	0.00	0.00
Upper	ASK14	0.00	0.22	0.01	0.00	0.00	0.00	0.16	0.00	0.00	0.62	0.38	0.00	0.00	1.00	0.00	0.00	0.00	0.00	0.00	0.00
	BSSA14	0.00	0.25	0.01	0.00	0.00	0.00	0.22	0.01	0.00	0.68	0.42	0.00	0.00	1.00	0.00	0.00	0.00	0.00	0.00	0.00
	CB14	0.00	0.34	0.05	0.00	0.00	0.00	0.35	0.03	0.01	0.75	0.47	0.00	0.00	1.00	0.00	0.00	0.00	0.00	0.00	0.00
	CY14	0.00	0.27	0.02	0.00	0.00	0.00	0.21	0.01	0.00	0.69	0.40	0.00	0.00	1.00	0.00	0.00	0.00	0.00	0.00	0.00
	I14	0.00	0.07	0.00	0.00	0.00	0.00	0.03	0.00	0.00	0.45	0.15	0.00	0.00	1.00	0.00	0.00	0.00	0.00	0.00	0.00

Note: Each of the five regions have different dominant seismic sources that are being tested by the PBR data. The dominant seismic source in Region 1 is the San Andreas fault. Region 2 is at the junction between the San Andreas, San Jacinto, and Transverse Ranges thrust faults. The dominant seismic sources in Region 3 is Pinto Mountain fault. Region 4 is between the San Andreas and San Jacinto faults. Region 5 is between the San Jacinto and Elsinore faults.